

Effect of surface hydraulics and salmon redd size on redd induced hyporheic exchange

Bishal Bhattarai¹, Brandon Hilliard¹, William Jeffery Reeder¹, Ralph Budwig¹, Benjamin T. Martin², Tao xing¹, and Daniele Tonina¹

¹University of Idaho

²Institute for Biodiversity and Ecosystem Dynamics, University of Amsterdam

December 7, 2022

Abstract

Salmonids bury their eggs in hyporheic streambed gravel, forming an egg nest, called a redd, characterized by a pit and a hump topography resembling a dune. Embryos' survival depends on downwelling oxygen-rich stream water fluxes, whose magnitudes are expected to depend on the interactions among redd shape, stream hydraulics, and the hydraulic conductivity of the streambed sediment. Here, we hypothesize that downwelling fluxes increase with stream discharge and redd aspect ratio, and such fluxes can be predicted using a set of dimensionless numbers, which include the stream flow Reynolds and Froude numbers, the redd aspect ratio, and the redd relative submergence. We address our goal by simulating the surface and subsurface flows with numerical hydraulic models linked through the near-bed pressure distribution quantified with a two-phase (air-water) two-dimensional surface water computational fluid dynamics model, validated with flume experiments. We apply the modeling approach to three redd sizes, which span the observed range in the field (from ~1 to ~4 m long), and by increasing discharge from shallow (0.1 m) and slow (0.15 m/s) to deep (8m) and fast (3.3 m/s). Results support our hypothesis of downwelling fluxes increasing with discharge and redd aspect ratio due to the increased near-bed head gradient over the redd. The derived equation may help evaluate the effect of regulated flow (e.g., hydroelectric and flood control dams) on redd-induced hyporheic flows.

Effect of surface hydraulics and salmon redd size on redd induced hyporheic exchange

Bishal Bhattarai¹, Brandon Hilliard², William J. Reeder², Ralph Budwig², Benjamin T. Martin³, Tao Xing^{1*} and Daniele Tonina²

1. Department of Mechanical Engineering, University of Idaho, Idaho, USA

2. Center for Ecohydraulics Research, University of Idaho, Idaho, USA

3. Institute for Biodiversity and Ecosystem Dynamics, University of Amsterdam, Amsterdam, the Netherlands

*Corresponding Author

ABSTRACT

Salmonids bury their eggs in hyporheic streambed gravel, forming an egg nest, called a redd, characterized by a pit and a hump topography resembling a dune. Embryos' survival depends on downwelling oxygen-rich stream water fluxes, whose magnitudes are expected to depend on the interactions among redd shape, stream hydraulics, and the hydraulic conductivity of the streambed sediment. Here, we hypothesize that downwelling fluxes increase with stream discharge and redd aspect ratio, and such fluxes can be predicted using a set of dimensionless numbers, which include the stream flow Reynolds and Froude numbers, the redd aspect ratio, and the redd relative submergence. We address our goal by simulating the surface and subsurface flows with numerical hydraulic models linked through the near-bed pressure distribution quantified with a two-phase (air-water) two-dimensional surface water computational fluid dynamics model, validated with flume experiments. We apply the modeling approach to three redd sizes, which span the observed range in the field (from ~1 to ~4 m long), and by increasing discharge from shallow (0.1 m) and slow (0.15 m/s) to deep (8m) and fast (3.3 m/s). Results support our hypothesis of downwelling fluxes increasing

24 with discharge and redd aspect ratio due to the increased near-bed head gradient over the redd. The
25 derived equation may help evaluate the effect of regulated flow (e.g., hydroelectric and flood control
26 dams) on redd-induced hyporheic flows.

27 **Keywords:**

28 hyporheic zone, salmon redd, flow discharge, downwelling flows

29 **Key statements:**

30 *(1) Redd-induced hyporheic exchange increases with discharge and redd aspect ratio*

31 *(2) Hyporheic downwelling flows are a function of surface Reynolds and Froude numbers and*
32 *redd aspect ratio*

33 *(3) Disturbed material hydraulic conductivity can be used to predict the downwelling flux*
34 *instead of categorical heterogeneity for the sediments*

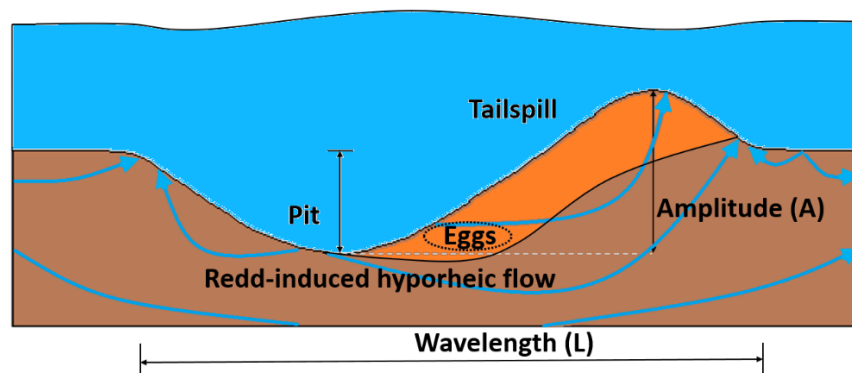
35

36 **1 INTRODUCTION**

37 Salmon females bury their eggs in streambed gravel, forming an egg nest (Crisp & Carling, 1989;
38 Deverall et al., 1993) having a typical dune-like shape (Figure 1). These dune-like features are
39 commonly referred to as a redd. To construct a redd the female excavates a hole, where she lays her
40 eggs, by redirecting the surface flow with her tail (Burner, 1951; Chapman, 1988; Groot & Margolis,
41 1991). These egg pockets can range from 15 to 50 cm in depth, depending on fish size, species, and
42 hydromorphological conditions (DeVries, 1997). After the eggs are fertilized by a salmon male,
43 female salmon cover them (forming the hump, Figure 1) with the sediment moved by digging a new
44 hole (forming the pit, Figure 1). This spawning activity results in a characteristic redd shape of a pit
45 followed by a hump, called the tailspill (Figure 1) (Bjornn & Reiser, 1991), which has a higher
46 permeability than the undisturbed sediments due to the winnowing away of fine grains and loosening

47 of the sediment matrix (Coble, 1961; Merz et al., 2004; Tappel & Bjornn, 1983; Zimmermann &
 48 Lapointe, 2005a). This shape resembles a dune, with an amplitude, A , equal to the difference in
 49 elevation between the bottom of the pit and the top of the tailspill, and its length, L , equal to the
 50 distance between the beginning of the pit and the end of the tailspill (Figure 1) (Crisp & Carling,
 51 1989; DeVries, 1997).

52 Salmonids may repeat their spawning activities several times resulting in more than one egg pocket in
 53 a single redd. In other cases, several spawners may use the same area to form superimposed redds
 54 (Hendry et al., 2004). Thus redd size may vary not only due to flow velocity and depth, excavating
 55 fish size, and sediment size (DeVries, 1997; Riebe et al., 2014), but also due to multiple spawning
 56 activities in the same location. This results in a potentially wide range of redd sizes from small redds
 57 of a few centimeters in amplitude and nearly 1 m long (e.g., sockeye salmon (*Oncorhynchus nerka*)
 58 (Hassan et al., 2015)) to large redds of decimeter amplitude and multiple meters in length (e.g.,
 59 Chinook salmon (*Oncorhynchus tshawytscha*) (Bjornn & Reiser, 1991; DeVries, 1997, 2012;
 60 Evenson, 2001; Tonina & Buffington, 2009a)). This size range may cause different hydrodynamic
 61 properties of the redd because of different aspect ratios, $A_R (= A/L)$ (Buxton, Buffington, Yager, et al.,
 62 2015), and different amplitudes protruding into the freestream flow.



63
 64
 65 Figure 1: Sketch of a longitudinal profile of a redd along the plane intersecting the center of the redd
 66 with expected hyporheic flow lines (modified from Tonina and Buffington (2009a)). Orange color
 67 indicates streambed material disturbed during spawning activity with higher hydraulic conductivity
 68 (K_D) than the undisturbed streambed (brown) material (K_{UD}).

69 Soon after spawning, the female salmon dies, while her embryos develop within the gravel over
70 several weeks (Bjornn & Reiser, 1991; Boyd et al., 2010). Their successful development depends on
71 hydrological and chemical characteristics within the redd (Bjornn & Reiser, 1991; Martin et al.,
72 2017), whose organic environment is supported by oxygen-rich stream waters entering, flowing
73 through, and exiting the streambed sediment (Coble, 1961; Cooper, 1965; Stuart, 1953b). This water
74 exchange is known as hyporheic exchange (Boano et al., 2014; Tonina & Buffington, 2009b) and
75 stems from the interaction between the freestream flow and the redd, causing large hydraulic head
76 gradients over upstream side of the tailspill, where stream water is driven into the sediment towards
77 the egg pocket (Figure 1), and low hydraulic heads near the tailspill crest, where hyporheic water
78 upwells back into the stream flow (Cardenas et al., 2016; Cooper, 1965; Stuart, 1953a) (Figure 1).
79 This redd-induced hyporheic exchange is shallower than and superimposed over hyporheic exchange
80 caused by large-scale streambed topography, like a pool and riffle (Tonina & Buffington, 2009a).
81 This exchange is assumed to be discharge-dependent (Cardenas et al., 2016), but as discharge
82 increases, both flow velocity and depth increase and their relative importance on redd-induced
83 hyporheic flows is not well understood. Since the redd morphology resembles a dune, Buxton et al.
84 (2015), recently modeled hyporheic flow through dunes using the equation of Elliot and Brooks
85 (Elliott, 1990; 1997b, 1997a) which were derived from Fehلمان's (1985) experiments for dune-like
86 bedforms. The Elliot and Brooks equation suggests an increase in pressure difference - and thus
87 hyporheic exchange - with an increase in velocity but a decrease with increasing water depth. Both
88 pressure and velocity increase with an increasing discharge, but their relative increase depend on
89 riverine morphology. Furthermore, Fehلمان's (1985) experiments had two similar dune sizes and
90 very narrow ranges of flow velocities and depths. In contrast, besides having broad size ranges and
91 aspect ratios, redd locations may experience shallow (a few centimeters) and deep (several meters)
92 mean flow depths with slow (a few centimeters per second) and fast (a few meters per second) mean

93 flow velocities. Consequently, the hydrological and morphological conditions of salmon redds go
94 beyond those modeled by Fehlman's (1985) experiments. Thus, the equation proposed by Elliot and
95 Brooks (Elliott, 1990; 1997a) may not be appropriate in predicting hyporheic exchange within redds
96 under flow scenarios different from the shallow and slow freestream velocities used in the
97 experiments.

98 This is an important limitation in predicting the impact of regulated flows (reservoir management or
99 water extraction) on embryo survival because of their dependence on downwelling velocities (Coble,
100 1961; Martin et al., 2020). Many salmonid species may spawn in river reaches downstream of
101 reservoirs, whose operations control stream discharge rather than headwater streams (Geist & Dauble,
102 1998; Yates et al., 2008). However, information on the impact of such management on redd habitat is
103 limited especially during drought years when water flow is curtailed.

104 We aim to address this knowledge gap and study the impact of redd size and surface hydraulics on
105 hyporheic flows within redds and the near-bed pressure gradient over redds. Based on previous
106 evidence (Cardenas et al., 2016; Fehlman, 1985; Tonina & Buffington, 2009a), we hypothesize that
107 downwelling fluxes increase with stream discharge and redd aspect ratio, and they can be predicted
108 from a set of dimensionless numbers, including the freestream flow Reynolds and Froude numbers,
109 the redd aspect ratio, and the redd relative submergence. We also investigate the effect of
110 heterogeneous (dual) hydraulic conductivities between disturbed (within the redd) and undisturbed
111 (surrounding streambed) sediments on hyporheic fluxes. We address our goal by simulating surface
112 and subsurface flows with two-dimensional numerical hydraulic models linked through the near-bed
113 pressure distribution quantified with a two-phase (air-water) surface water computational fluid
114 dynamics model. We applied the modeling approach to five redd sizes with L, M, S, VS and ES
115 identifying the large, medium, small, very small and extremely small, which span the observed range
116 in the field (from ~1 to ~4 m long) (Bjornn & Reiser, 1991; DeVries, 1997, 2012; Evenson, 2001;

117 Tonina & Buffington, 2009a) and imposed stream discharges spanning from shallow (0.1 m) and
118 slow (0.15 m/s) to deep (8 m) and fast (3.3 m/s) waters. The paired depth-velocity values were
119 selected from those observed near redd locations along the Sacramento River (California, USA)
120 downstream of the Shasta dam. Results support our hypothesis of downwelling fluxes increasing with
121 discharge or redd aspect ratio due to an increase in the near-bed head gradient over the redd.

122 **2 METHODS**

123 We used a two-dimensional (2D) computational fluid dynamics (CFD) model (ANSYS®) to simulate
124 surface (Reynolds averaged Navier Stokes equation, RANS) and groundwater (Darcian flow)
125 hydraulics numerically. The two domains were simulated separately and linked via the near-bed
126 pressure distribution (Janssen et al., 2012) induced by 2D simplified salmon redds (Cardenas et al.,
127 2016), whose dimensions span those found in the literature. The surface model was validated by
128 comparing CFD results with laboratory measurements of near-bed pressures from Fehlman (1985) as
129 done by others (Cardenas & Wilson, 2007; Reeder et al., 2018; Trauth et al., 2013) and by data from
130 experiments in our salmon redd physical model. The results from the surface and subsurface models
131 were interpreted with a set of dimensional numbers to generalize the results for the pressure drop
132 around the redd and the interstitial downwelling fluxes through the redd (Monofy & Boano, 2021).

133 **2.1 Surface flow hydraulics**

134 Open flow surface hydraulics were modeled by solving the RANS equations with a κ - ϵ realizable
135 turbulence closure scheme incorporated within the finite volume ANSYS software program. This
136 turbulence closure was chosen because of its higher performance over other schemes in terms of
137 predicting flows with strong streamlines curvature, flow separations and flows with complex
138 secondary flow features (*ANSYS Fluent Theory Guide*, 2019). Surface water elevation of open
139 channel flows with the fixed lid approach (Janssen et al., 2012), which prescribes the water surface

140 elevation with an impermeable, slip, and no-shear wall condition, may not properly capture the spatial
141 gradients that are present in open flows (Meselhe & Odgaard, 1998; Monsalve & Yager, 2017). As a
142 result, we treated the system as a two-phase (air and water) problem and tracked the water surface
143 elevation at the air-water interface using the volume of fluid (VOF) approach (Hirt & Nichols, 1981).
144 The water surface profile was extracted at locations where the volume fraction is 0.5, where values of
145 1 or 0 represent only water or air, respectively. We used a long flow domain with two fixed-lid
146 sections upstream and downstream of a 45 m long two-phase domain to train and develop the flow
147 (Figure 2a). We ran all simulations for at least two flow cycles throughout the full domain to ensure
148 that the flows were in equilibrium with the boundary conditions. The water-sediment interface was
149 specified as a no-slip impermeable boundary, which is a typical condition for this problem (Cardenas
150 & Wilson, 2007b; Chen et al., 2015), because momentum and mass exchanges with porous sediment
151 are small and have negligible influence on surface hydraulics (Janssen et al., 2012). Water boundaries
152 were defined as velocity inlet and velocity outlet conditions for the upstream and downstream
153 locations respectively, whereas air boundaries were specified as pressure outlets. The entire domain
154 was sloped to resemble a streambed gravity flow (Elliott & Brooks, 1997b; Fehlman, 1985). There
155 are approximately two million quadrilateral cells with a mean cell size of about 2.4 cm in the
156 horizontal direction. We employed a highly refined 1.5 mm cell size in the vertical direction at the
157 air-water interface to accurately track water surface elevation and a very small vertical cell size of
158 about 0.1 mm near the bottom boundary (Figure 2b). We ran mesh independence tests with three
159 different mesh sizes (fine, medium, and coarse) by reducing the mesh dimensions by 30%, and
160 compared their predicted pressure distributions, which resulted in a change of total head drop through
161 the redd of less than 3% from the fine to coarse mesh. Therefore, all simulations were conducted with
162 the medium mesh to save computational cost.

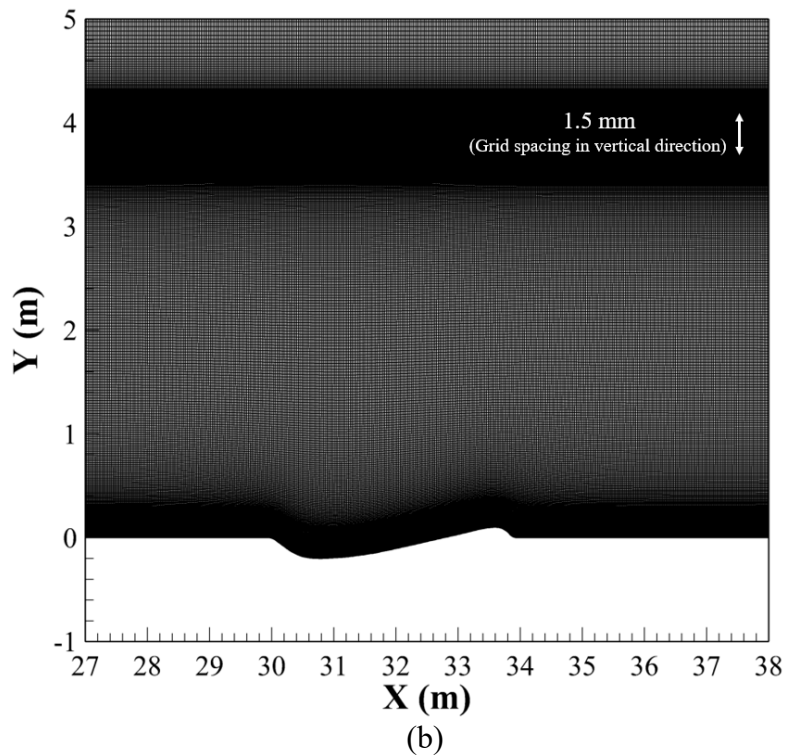
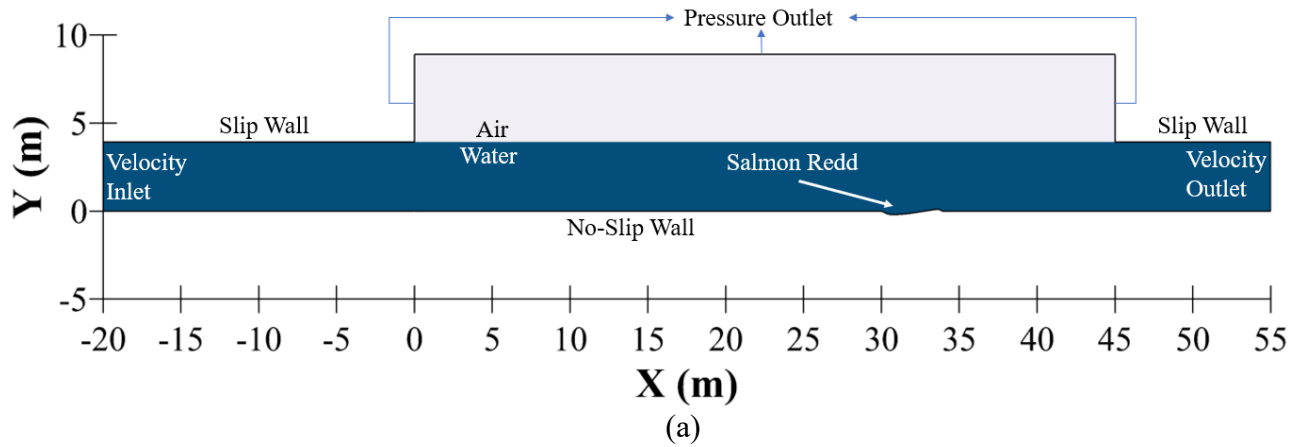


Figure 2: Simulation domain design: (a) surface flow domain with air colored in grey and water colored in blue along with the boundary conditions, and (b) Zoomed-in section near the redd showing the mesh.

169 2.2 Groundwater flow hydraulics

170 A steady-state Darcian groundwater flow was solved to predict the redd-induced interstitial flows
 171 (Cardenas et al., 2016; Tonina & Buffington, 2009a) in ANSYS. The water-sediment interface was
 172 defined as a pressure inlet boundary with the specified pressure distribution predicted from the CFD
 173 surface model. A periodic boundary condition, which simulates an infinite periodic domain, was

174 applied at the upstream and downstream locations of the subsurface domain boundaries with an
175 ambient groundwater flow of nearly 0.001 mm/s, which mimics a large-scale longitudinal
176 groundwater underflow caused by a valley slope. The bottom boundary was treated as a no-slip
177 impermeable wall positioned five meters below the flat water-sediment interface to not affect the
178 redd-induced hyporheic flow. The average grid cell size was 2.5 cm horizontally and 1.5 cm
179 vertically, resulting in approximately one million quadrilateral cells. The permeability, k , was set to
180 be homogenous and isotropic, with a value of $5.1 \cdot 10^{-11} \text{ m}^2$, equivalent to a hydraulic conductivity of
181 $K = 0.0005 \text{ m/s}$.

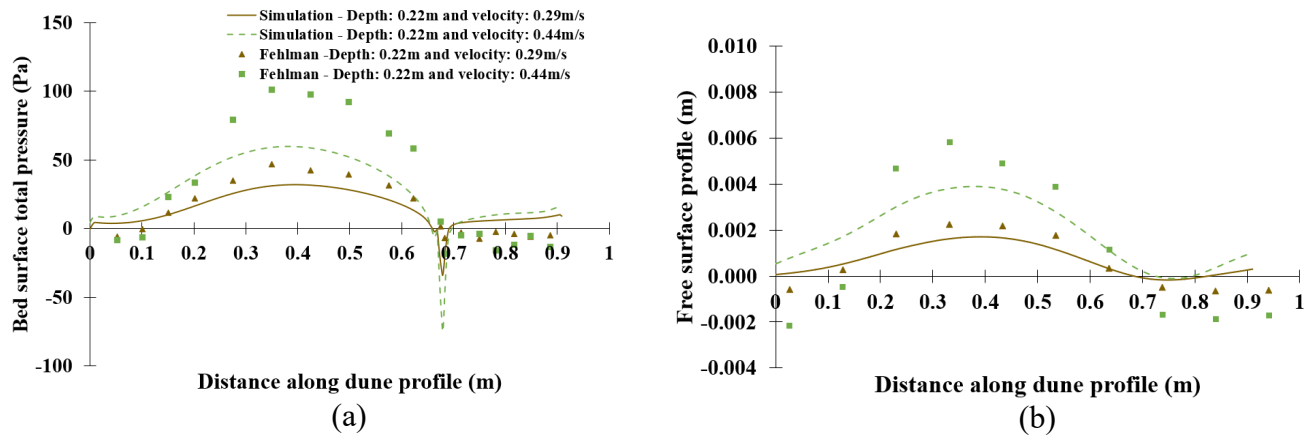
182 Due to the winnowing of fine material and loosening of the sediment matrix during the redd
183 construction, newly formed redds have a higher hydraulic conductivity, K_D (disturbed sediment), than
184 that of the undisturbed streambed material, K_{UD} (undisturbed sediment). These two different
185 hydraulic conductivities form a categorical heterogeneous system, which may result in higher mean
186 downwelling flow than the homogenous case. To investigate this possibility, we studied a case of
187 categorical heterogeneity for run 14, M (Table 4), a medium redd with surface flow depth of 3.92 m
188 and velocity of 1.49 m/s. The hydraulic conductivity within the redd, ($K_D = 5 \cdot K_{UD}$ and $10 \cdot K_{UD}$) was
189 increased by half an order of magnitude and one full order of magnitude as documented in the
190 literature (Zimmermann & Lapointe, 2005a) from that of the surrounding undisturbed sediment (K_{UD}
191 $= K = 0.0005 \text{ m/s}$) (Figure 1). Because hyporheic flow is chiefly a near-surface process, we
192 hypothesized that the hydraulic conductivity of the redd would dominate the redd-induced hyporheic
193 flows and thus the effect of categorical heterogeneity between the disturbed and undisturbed sediment
194 would be negligible, causing the system to be treated as homogenous with the hydraulic conductivity
195 of the redd as the reference property. This heterogeneity is different from the internal heterogeneity
196 caused by the redd internal architecture which may form zones of progressive lower hydraulic
197 conductivity from the egg pocket to the redd surface (Chapman, 1988).

198 **3 CFD SIMULATIONS VERIFICATION AND VALIDATION**

199 We validated the CFD modeling by comparing flow hydraulics predicted by the model with those
200 measured in the flume experiments with dune bedforms conducted by Fehlman (1985) as well as
201 those of a redd bedform conducted by us in this study. We also quantified uncertainty due to
202 measurement errors and validated the mesh and time-step used in the simulations.

203 **3.1 Fehlman's (1985) flume experiments**

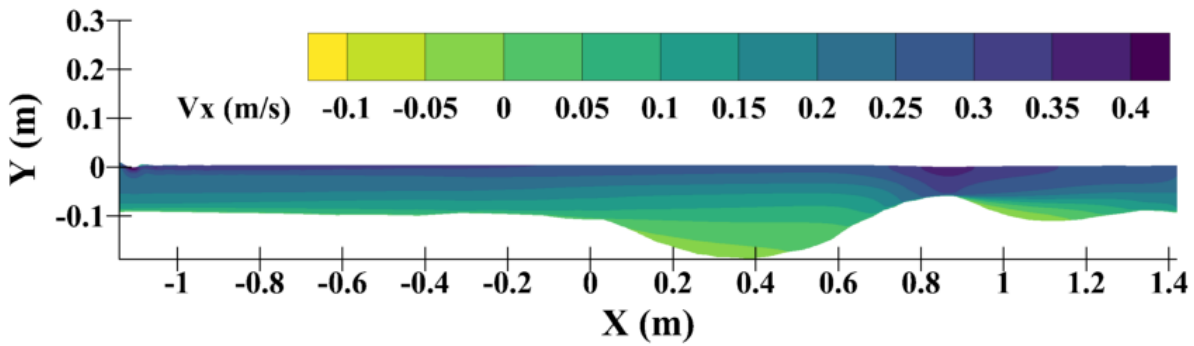
204 Redds have similar geometry to dunes, so we used Fehlman's (1985) data set which contains pressure
205 distributions over dunes to validate the CFD modeling. We selected two experiments that have the
206 same average flow depth of 0.22 m but two distinct average flow velocities of 0.29 m/s and 0.44 m/s
207 (Fehlman, 1985). We simulated the entire flume experiment as an open channel flow and extracted
208 the pressure and water surface profiles at the 8th (center) dune, out of 15 consecutive dunes as done
209 experimentally by Fehlman (1985). Simulation performance was quantified with Nash-Sutcliffe
210 coefficients (NSC) whose values indicate the quality of the model performance: very good (NSC >
211 0.75), good (0.65 < NSC ≤ 0.75), satisfactory (0.5 < NSC ≤ 0.65), and unsatisfactory (NSC ≤ 0.5)
212 (Moriassi et al., 2007). The accuracy of the comparison by visual inspection between predicted and
213 measured pressure distributions (Figure 3a) is comparable to that reported in the literature (Cardenas
214 et al., 2016; Reeder et al., 2018). The NSC of 0.7 and 0.6 for flows with velocity 0.29 m/s and 0.44
215 m/s respectively also support the visual inspection. Unlike previous studies, we also modeled the
216 respective water surface elevations to those reported by Fehlman (1985) with NSC values of 0.8 and
217 0.7 (Figure 3b).



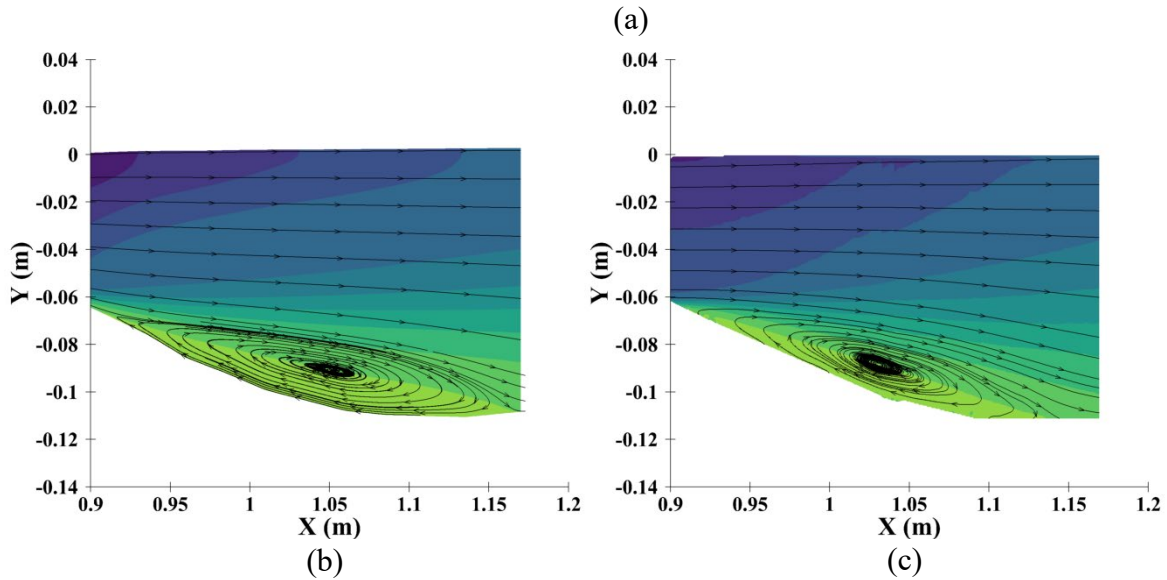
218
 219
 220 Figure 3: Comparison between simulations (lines) and Fehلمان's experiments (symbols) for (a) total
 221 pressure and (b) free surface profiles at the 8th dune.

222 3.2 Redd experiments

223 We conducted four experimental runs with four combinations of upstream flows: two depths of
 224 shallow (0.1 m) and deep (0.2 m) water and two velocities of slow (0.1 m/s) and fast (0.2 m/s) flow in
 225 a 7 m long, 0.5 m wide, and 0.7 m deep recirculating flume (Table 1) at the Center for Ecohydraulics
 226 Research (Bhattarai et al., 2022; Moreto et al., 2022). The redd, which was a ¼-scaled version of an
 227 average redd was made with THV grains which are on the order of 3 mm in nominal diameter. The
 228 rest of the sediment was made with crashed glass of about 3 mm in size. The redd was placed in the
 229 middle section of the flume to minimize boundary effects. The water passed through a flow
 230 straightener before entering the flume while a weir gate regulated the downstream boundary. Stereo
 231 Particles Image Velocimetry, or SPIV, was used to map the flow field downstream of the redd crest
 232 where complex hydraulics occur to validate the CFD model. We collected the flow field from the
 233 upstream at $x = -1.14$ m and the downstream at $x = 1.42$ m to define boundary conditions for the
 234 streamwise (V_x) and vertical (V_y) velocities (V_y was less than 2% of V_x) and turbulence kinetic
 235 energy (TKE) profiles for the CFD models (Figure 4a). 2,000 image pairs were collected during the
 236 SPIV experiments, which ensured ergodicity of the flow field (Moreto et al., 2022).



237



238

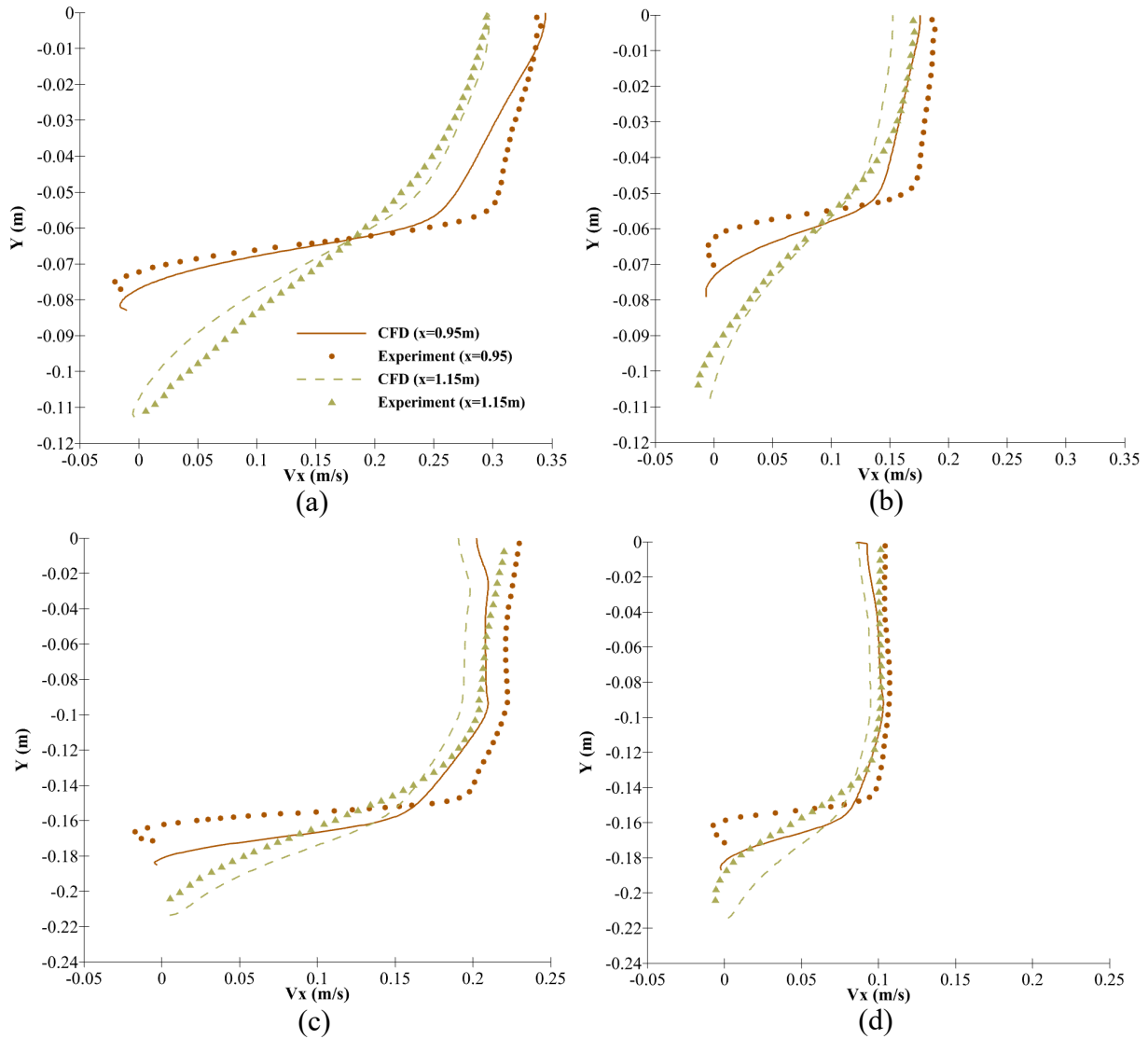
239 Figure 4: Velocity field for the shallow-fast case for (a) the entire simulation domain and (b) close-up
 240 views downstream of the redd crest simulated by CFD and (c) measured with stereo particle image
 241 velocimetry.

242 Table 1. Four experimental flow conditions used as CFD boundary conditions, with average depths
 243 (averaged between the upstream and downstream), average velocities, and average TKE.

Runs Description	Avg Depth (m)	Avg velocity (V_x) (m/s)		Avg TKE (m^2/s^2) $\times 10^{-4}$	
		Upstream	Downstream	Upstream	Downstream
Shallow-fast	0.105	0.191	0.209	2.13	20.4
Shallow-slow	0.098	0.103	0.109	0.638	6.18
Deep-fast	0.1974	0.175	0.169	0.933	4.77
Deep-slow	0.1972	0.085	0.081	0.194	1.26

244 Comparisons of the overall size of the separation vortex and reattachment locations show very good
 245 agreement between the measured and CFD predicted flow fields downstream of the redd (Figure 4b
 246 and Figure 4c). Comparisons between x-velocity profiles just downstream of the crest ($x = 0.95$ m)
 247 and near the bottom of the hump (1.15 m) for all four flow cases give very good NSC values of 0.954

248 and 0.969 for the shallow-fast flow, 0.824 and 0.967 for shallow-slow flow, 0.644 and 0.923 for
249 deep-fast flow, and 0.6 and 0.845 for deep-slow flow at $x = 0.95$ m and $x = 1.15$ m, respectively
250 (Figure 5). This confirms that our CFD model adequately predicted the flow field caused by the redd-
251 flow interaction.



252

253

254 Figure 5: Comparison between the simulated (solid and dash) and experimental (symbols) x-velocity
255 profiles at $x = 0.95$ m and 1.15 m for (a) shallow-fast, (b) shallow-slow, (c) deep-fast, and (d) deep-
256 slow flows.

257 3.3 Mesh size, time-step resolution, and flow uncertainty validation

258 To ensure that the results are independent of mesh and time-step resolutions, we performed a solution
 259 verification for V_x on three systematically refined meshes (fine, medium, and coarse) for the shallow-
 260 fast flow case, which is the most critical one. The overall grid size, total number of grid points, and
 261 time step size used are given in Table 2. We used a grid refinement ratio, $r_G = \Delta x_2 / \Delta x_1 =$
 262 $\Delta x_3 / \Delta x_2 = 1.414$, where Δx is the grid distance between two elements and the subscripts 1, 2, and 3
 263 represent the fine, medium, and coarse meshes, respectively. The overall procedure is as described in
 264 (Xing et al., 2008; Xing & Stern, 2010, 2011). The convergence ratio, denoted by R_G , is the ratio of
 265 solution differences for medium-fine and coarse-medium solution pairs. L2 norms of x-velocity
 266 profiles are used to calculate $\varepsilon_{G_{21}}$ and $\varepsilon_{G_{32}}$ to define the ratios for R_G and P_G (observed order of
 267 accuracy), i.e.,

268

$$\langle R_G \rangle = \|\varepsilon_{G_{21}}\|_2 / \|\varepsilon_{G_{32}}\|_2 \quad (1)$$

$$\text{where } \|\varepsilon_{G_{21}}\|_2 = \sqrt{\sum_{k=1}^N (P_1 - P_2)^2} \quad (2)$$

$$\langle P_G \rangle = \frac{\ln(\|\varepsilon_{G_{32}}\|_2 / \|\varepsilon_{G_{21}}\|_2)}{\ln(r_G)} \quad (3)$$

269 where $\langle \rangle$ & and $\|\cdot\|_2$ denotes a profile-averaged quantity (solution change ratio based on L2 norms)
 270 and L2 norm, respectively (Wilson et al., 2001). N is the number of points along a single velocity
 271 profile and P_1 and P_2 are the point solutions (V_x) for meshes 1 and 2, respectively. U_G is the
 272 numerical uncertainty estimate and $|E|$ is the absolute relative error between the fine mesh and the
 273 experimental data, representing a measure of bias error between the numerical and experimental
 274 results ($|E| = |S - D|$), where S is the fine mesh streamwise average velocity, and D is the

275 experimental streamwise average velocity. U_V is the validation uncertainty ($U_V = \sqrt{U_G^2 + U_D^2}$), where
 276 U_D is the experimental uncertainty, representing an average uncertainty of the numerical and
 277 experimental results. Validation is achieved when $|E| < U_V$.

278 Table 2. Solution verification.

Grids	Grid Dimensions	Total Number of Points	Time step size
1	869 × 220	191,180	0.002
2	615 × 155	95,325	0.002828
3	430 × 108	46,440	0.004

279
 280 For the solution verification and validation study, we used four locations ($x = 1$ m, 1.05 m, 1.1 m, and
 281 1.15 m). The grid triplet showed monotonic convergence ($0 < R_G < 1$) at all horizontal locations with
 282 small grid uncertainty values ranging from 31.7 %D to 62.5 %D. All four locations showed that the
 283 model was validated ($|E| < U_V$) in (Table 3).

284 Table 3. Verification & Validation study for the longitudinal component of the velocity. Percentages
 285 are calculated using experimental data (%D).

x-location (m)	R_G	P_G	U_G	U_G (%D)	U_D (%D)	 E (%D)	U_V (%D)
1.0	0.23	2.07	0.0695	31.69	0.33	1.36	31.7
1.05	0.24	2.05	0.0638	32.68	0.41	2.56	32.68
1.1	0.27	1.87	0.066	36.17	0.5	3.57	36.17
1.15	0.39	1.36	0.11	62.53	0.55	2.70	62.53

286

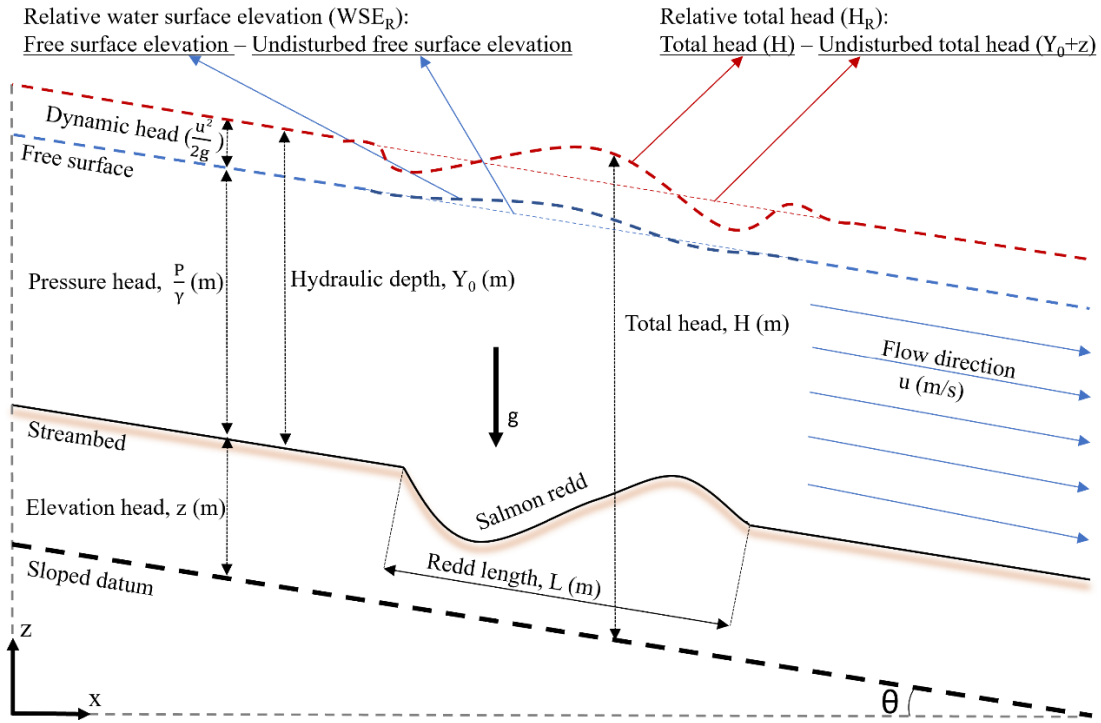
287 4 FLOW SCENARIOS

288 We developed a set of 32 flow simulations using paired mean flow depth and velocity values
 289 obtained at redd locations along the Sacramento River for Chinook salmon (*Oncorhynchus*
 290 *tshawytscha*) (Table 4) (Data from NOAA, Andrew Pike, Winter-run Chinook salmon Lifecycle
 291 model project, see data repository). The Sacramento River data (19 velocity-depth sets) were
 292 augmented with one set of surface water information from the Columbia River (Mueller, 2005), six
 293 sets of Fehlman's (1985) flume experimental runs, two sets from Deverall's (1993) field data, and

294 four additional depth-velocity sets to increase the range to shallower flow conditions than those
295 observed in the data of the Sacramento River. We used three redd sizes to account for their natural
296 variation: large, medium, and small, with lengths of 3.9, 2.8, and 1.82 m and aspect ratios of 0.077,
297 0.139, and 0.265, respectively (Deverall et al., 1993; Evenson, 2001; Tonina & Buffington, 2009a).
298 These three sizes were augmented with two additional smaller redd sizes for shallow water conditions
299 to mimic egg nests built by salmonids, such as sockeye salmon (*Oncorhynchus nerka*) smaller than
300 Chinook salmon. The smaller redds had wavelengths of 1.0 m and 0.914 m, with aspect ratios of
301 0.139 and 0.15, respectively.

302 **5 DATA ANALYSIS**

303 We expressed pressure (P) as pressure head with a unit of meters of water, i.e., P/γ , where γ is the
304 specific weight of water. To compare the distributions among all scenarios, we removed the effect of
305 the hydrostatic pressure over the undisturbed inclined bed and the local slope by defining the relative
306 total head, $H_R = H - (Y_0 + z)$, where H is the total head, Y_0 is the undisturbed hydraulic depth away from
307 the redd based on the inlet water depth and z is the difference between the local streambed and the
308 datum that are sloped at the same angle (Figure 6). This is similar to Fehlman's (1985) approach, but
309 while he referenced the pressure to the depth at the dune crest, we used Y_0 and mean flow velocity, u ,
310 upstream enough from the redd as a reference value. These values would be similar to those
311 quantified at the reach scale which would be available through one-dimensional hydraulic modeling
312 or discharge field surveys. The use of H_R eliminates the influence of the large static pressure (Y_0)
313 running over small near-bed pressure variations and mean streambed slope for all simulations,
314 allowing visualization of the pressure difference from its mean value. This pressure gradient induces
315 the hyporheic exchange (Elliott & Brooks, 1997b) (Figure 1). The relative water surface elevation
316 (WSE_R) is defined as the difference between the local free surface elevation and the undisturbed free
317 surface elevation based on water depth at inlet (Figure 6).



319

320

321 Figure 6: An illustration of all heads flowing across the redd in an open channel flow (the slope angle
 322 is so small such that the water depths in the vertical direction z and normal direction of the slope are
 323 functionally identical).

324 6 DIMENSIONAL ANALYSIS

325 From a dimensional analysis of the problem, we found that the redd-induced total head drop, $\Delta H_R =$
 326 $H_{R,H} - H_{R,L}$, with $H_{R,H}$ and $H_{R,L}$ being the maximum and minimum relative total heads over the redd,
 327 respectively, depends on seven quantities: mean cross-sectional velocity, u , undisturbed hydraulic
 328 depth, Y_0 , gravity, g , dynamic viscosity, μ , the density of water, ρ , redd amplitude, A , and redd length,
 329 L . The application of the Buckingham theorem reduces them to a set of five dimensionless groups,
 330 which are the pressure gradient, $H^* = \frac{\Delta H_R}{L}$, the redd aspect ratio, A_R , the redd relative submergence,
 331 A/Y_0 , freestream Reynolds number, $Re = \frac{u \cdot Y_0}{\nu}$ and the freestream Froude number, $Fr = \frac{u}{\sqrt{g \cdot Y_0}}$. A
 332 similar analysis to predict the spatially averaged hyporheic downwelling fluxes over the entire redd,
 333 \bar{q}_d , and over the portion that delivers oxygen-rich surface water to the egg pocket, $\bar{q}_{d,ep}$, (both

334 normalized by the redd hydraulic conductivity (K) of the streambed sediment, $\bar{q}_d^* = \bar{q}_d/K$ and
335 $\bar{q}_{d,ep}^* = \bar{q}_{d,ep}/K$) yields the same set of dimensionless independent variables. The dimensionless
336 downwelling velocity, q_d^* , also allows comparison between the homogenous and categorical
337 heterogeneous hydraulic conductivity cases. When homogeneous q_d^* are plotted against those of the
338 heterogeneous cases and fall on a 1:1 line, the system behaves linearly and supports our hypothesis.
339 In our analysis, we did not consider the alluvium depth a hindrance and thus we neglected it. We
340 performed regression analysis to characterize the functional relationship between the dependent
341 dimensionless variables and the set of independent dimensionless variables, e.g., $H^* = f(Re, Fr, A_R,$
342 $A/Y_0)$. The simulations were split into two groups, one with 21 simulations to develop regression
343 curves and the other with 27 simulations to validate the curves.

344

345

346

347

348

349

350

351

352

353

354

355

356

357 Table 4. Summary of surface flow characteristics and redd sizes with L, M, S, VS and ES identifying
 358 the large, medium, small, very small, and extremely small sizes of 3.9, 2.8, 1.82, 1 and 0.914 m
 359 wavelengths and with aspect ratios of 0.077, 0.139, 0.265, 0.139 and 0.15 respectively (Deverall et
 360 al., 1993; Evenson, 2001; Tonina & Buffington, 2009a). The 21 simulations utilized for validation
 361 from the independent set of calibration are marked with an asterisk (*) on the redd size. The data
 362 source for velocity-depth paired values are (Fehlman, 1985), (Deverall et al., 1993), Columbia River
 363 (Mueller, 2005) and Sacramento River (Data from NOAA, Andrew Pike, Winter-run Chinook salmon
 364 Lifecycle model project).

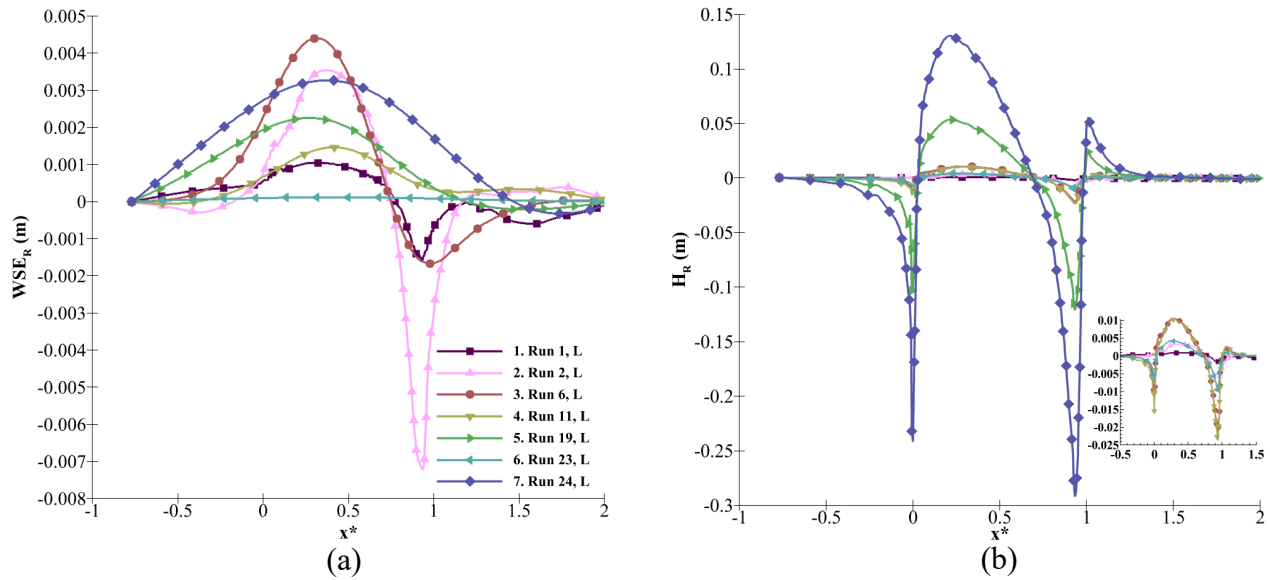
Run Number	Flow Depth (m)	Velocity (m/s)	Froude Number (Fr)	Reynolds Number (Re)	Redd Size	Source
1	0.25	0.15	0.10	37158	L*	Fehlman
2	0.25	0.29	0.19	72829	L*	Fehlman
3	0.38	0.58	0.30	218913	L, M*, S	Deverall
4	0.75	0.35	0.13	260729	L	Deverall
5	1.14	0.68	0.20	764308	L	Sacramento river
6	1.67	0.91	0.23	1514422	L	Sacramento river
7	1.94	0.40	0.09	761129	L*, M, S*	Sacramento river
8	2.06	1.12	0.25	2291632	L	Sacramento river
9	2.31	0.59	0.12	1351410	L, M*, S	Sacramento river
10	2.47	1.28	0.26	3140267	L	Sacramento river
11	2.88	0.91	0.17	2597395	L*, M, S*	Sacramento river
12	3.30	1.69	0.30	5539369	L	Sacramento river
13	3.47	1.27	0.22	4377164	L*	Sacramento river
14	3.92	1.49	0.24	5801389	L, M*, S	Sacramento river
15	4.04	1.90	0.30	7624205	L	Sacramento river
16	4.39	1.68	0.26	7325435	L	Sacramento river
17	4.73	2.03	0.30	9537110	L	Sacramento river
18	4.84	1.85	0.27	8893582	L	Sacramento river
19	5.22	2.00	0.28	10369555	L*, M, S*	Sacramento river
20	5.69	2.21	0.30	12490049	L	Sacramento river
21	6.51	2.60	0.33	16811790	L, M*, S	Sacramento river
22	7.03	2.87	0.35	20039960	L	Sacramento river
23	7.30	0.60	0.07	4350445	L	Columbia river
24	7.95	3.26	0.37	25742122	L*, M*, S	Sacramento river
25	0.1	0.15	0.15	14899	VS*	This study
26	0.1	0.3	0.3	29798	VS	This study
27	0.2	0.15	0.11	29798	VS*	This study
28	0.2	0.3	0.21	59595	VS	This study
29	0.27	0.16	0.10	44118	ES*	Fehlman
30	0.22	0.29	0.2	64715	ES*	Fehlman
31	0.32	0.36	0.2	114040	ES*	Fehlman
32	0.27	0.49	0.3	132272	ES*	Fehlman

366 7 RESULTS

367 7.1 Modeled surface flow

368 Both relative water surface elevation, WSE_R , (Figure 7a) and relative total head, H_R , (Figure 7b) over
369 the redd depend on flow depth and velocity. For the same water depth, both WSE_R and H_R amplitudes
370 increase with stream velocity (Figure 7, compare runs 1 and 2). However, when keeping the same
371 velocity, the H_R amplitude tends to remain constant with increasing depth, whereas WSE_R amplitude
372 decreases with increasing depth (circle and downward triangle, runs 6 and 11). The deepest and
373 fastest flow (diamond, run 24) causes the largest H_R amplitude over the redd (Figure 7b). As observed
374 for dune-like bedforms, discharge regulates the magnitude of the pressure amplitude, which increases
375 with discharge, but the shape of the pressure distribution remains the same regardless of discharge.
376 Unlike dunes, which have only one minimum and one maximum pressure, redds have two minima,
377 one at the head of the pit and one at the crest, and two maxima, one near the middle of the tailspill,
378 and the other downstream of the crest, where the redd ends at the undisturbed bed (Figure 7b). The
379 lowest minimum near-bed pressure occurs at the crest of the redd, and the highest near-bed pressure
380 occurs along the middle of the tailspill.

381

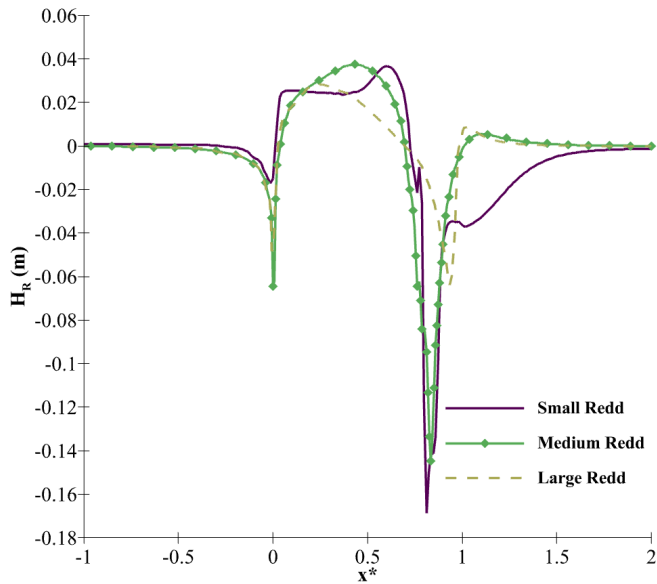


382
383
384
385
386

Figure 7: (a) Relative water surface elevation (WSE_R) and (b) Relative total head (H_R) as a function of dimensionless distance x^* , defined as the distance normalized by redd wavelength ($x^* = x/L$), over the large redd size (3.9 m).

387 Redd aspect ratios affect the pressure drop magnitude, and large A_R values (~ 0.265) also have a
388 profound impact on the shape of the pressure profile (Figure 8). The magnitude of the second
389 maximum near-bed pressure value, which lies downstream of the crest, decreases as A_R increases
390 until it disappears for A_R values between 0.14 and 0.26.

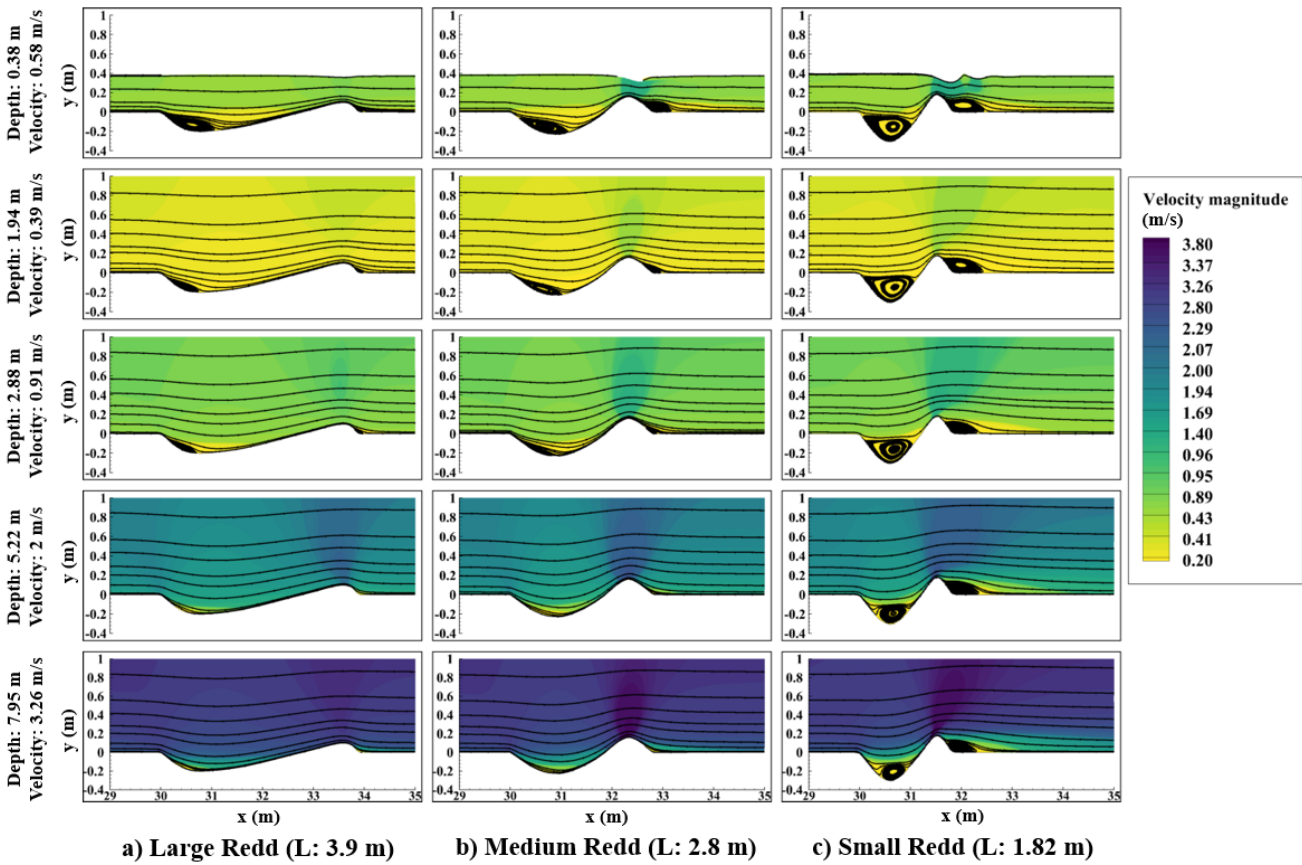
391 The interaction between surface flows and redd shapes and sizes (A_R) affect the flow velocity with
392 stronger near-bed velocity gradients as either discharge or A_R increases (Figure 9). For each discharge
393 and A_R , the highest velocity occurs on the crest of the redd, and the slowest velocity occurs in the pit.
394 Another low velocity is detected just downstream of the redd's lee side. The size of the separation
395 vortices within the pit increases as the surface flow velocity increases. The same is true with
396 decreasing redd size, even for the same discharge. Another flow recirculation is developed just
397 downstream of the tailspill for the smallest redd indicating that increasing discharges and A_R values
398 result in increasing pressure amplitudes over the redd. This process causes a systematic increase of
399 the total head drop, H^* , with an increase in the Reynolds, Froude, and A_R numbers (Figure 10).



400
401
402
403

Figure 8: Relative total head (H_R) over three redd sizes (Small = 1.82 m, Medium = 2.8 m, and Large = 3.9 m) for Run 14. Aspect Ratios are $A_R = 0.265$, 0.139 and 0.077 , respectively.

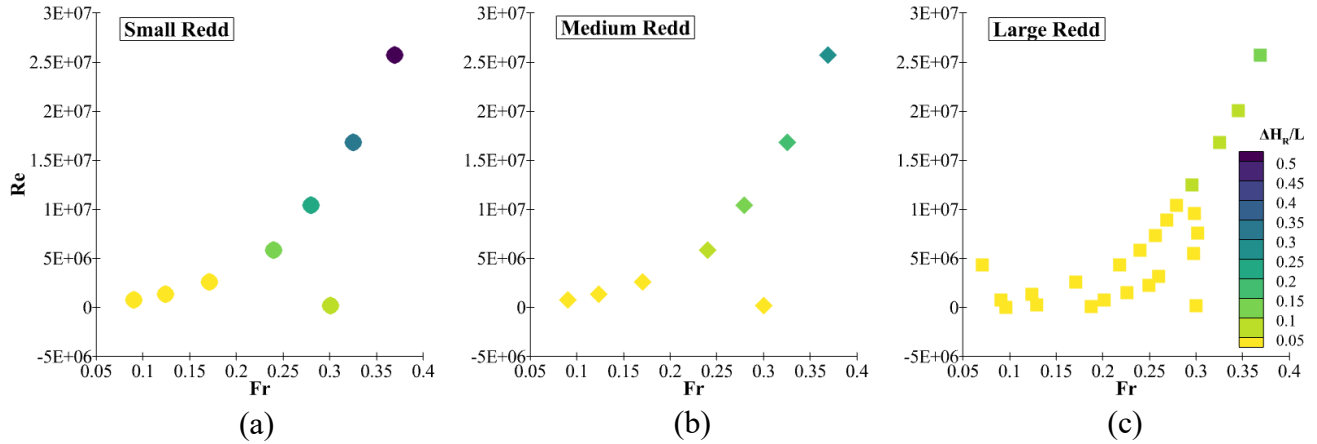
404



405
406
407

Figure 9: Surface flow characteristics for different surface hydrodynamics and different redd sizes.

408



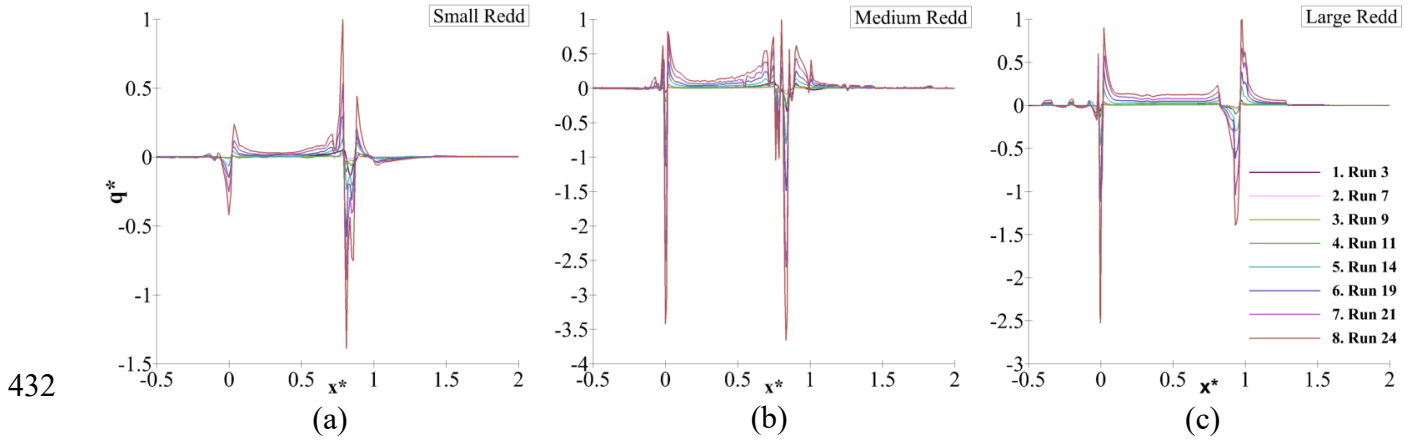
409

410 Figure 10: Dimensionless total head ($\Delta H_R/L$) as a function of Reynolds Number (Re), Froude Number
 411 (Fr), and Redd Aspect Ratio (A_R). Aspect Ratios are $A_R = 0.265$, 0.139 , and 0.077 for small, medium,
 412 and large redd respectively.

413 7.2 Modeled hyporheic flow

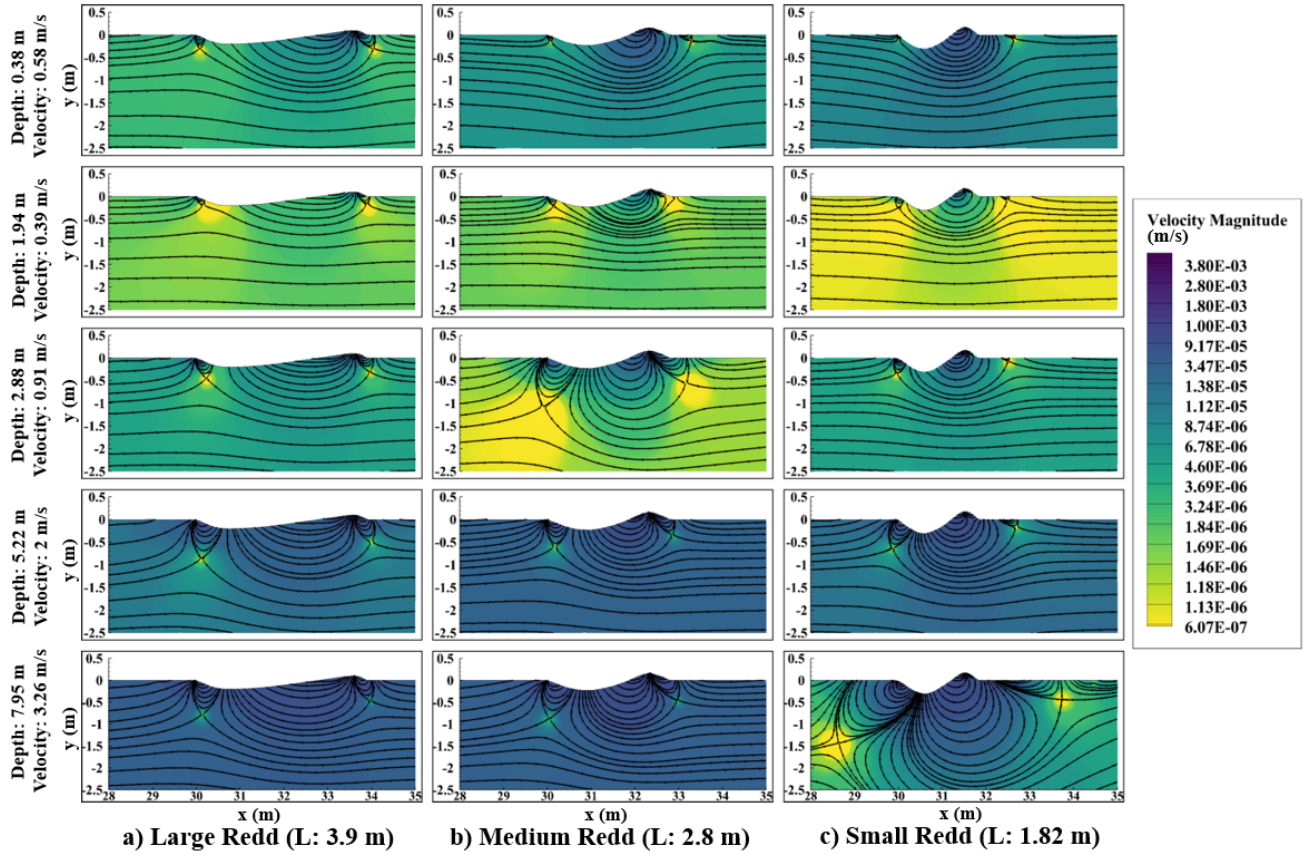
414 Upwelling and downwelling fluxes, forming the hyporheic exchange, increase with discharge as seen
 415 in the increase in the normalized normal velocity distribution, $q^* = q/q_{max}$, defined as the normal
 416 velocity distribution (normal to the water bed surface) normalized by its maximum value, over the
 417 redd for different flow velocities and depths (Figure 11). q_{max} for small, medium and large redds are
 418 0.00396 m/s, 0.0009 m/s and 0.00068 m/s, respectively. As with H_R , their magnitude decreases as
 419 water depth and velocity decrease. The highest redd aspect ratio gives rise to the maximum hyporheic
 420 exchange, the largest hyporheic cell size, and the highest downwelling velocity. High upwelling
 421 (negative normal velocity) and downwelling velocities are seen in the same locations as the high H_R
 422 values (compare Figure 7 and Figure 11). The surface flow-redd interaction formed three to four
 423 recirculating cells: one large cell with a downstream flow direction between the redd trough and crest,
 424 two with an upstream flow direction (one below the pit and one at the crest), and one slightly
 425 downstream of the crest (upstream flow direction) that did not appear for low A_R (Figure 12). The
 426 main hyporheic flow cell, which brings oxygen-rich surface water to the egg nest (see Figure 1 for
 427 potential locations of the egg pocket), has most of the flux upwelling at the crest's low-pressure zone,

428 while a portion is entrained by the underflow and does not return to the river. Between slightly
 429 downstream of the pit and upstream of the tailspill of the redd, the flow reaches the egg pocket before
 430 arching back to the streambed surface. Both spatially averaged downwelling velocities (\bar{q}_d , and $\bar{q}_{d,ep}$)
 431 systematically increase with the larger Reynolds and Froude numbers, as well as redd A_R (Figure 13).



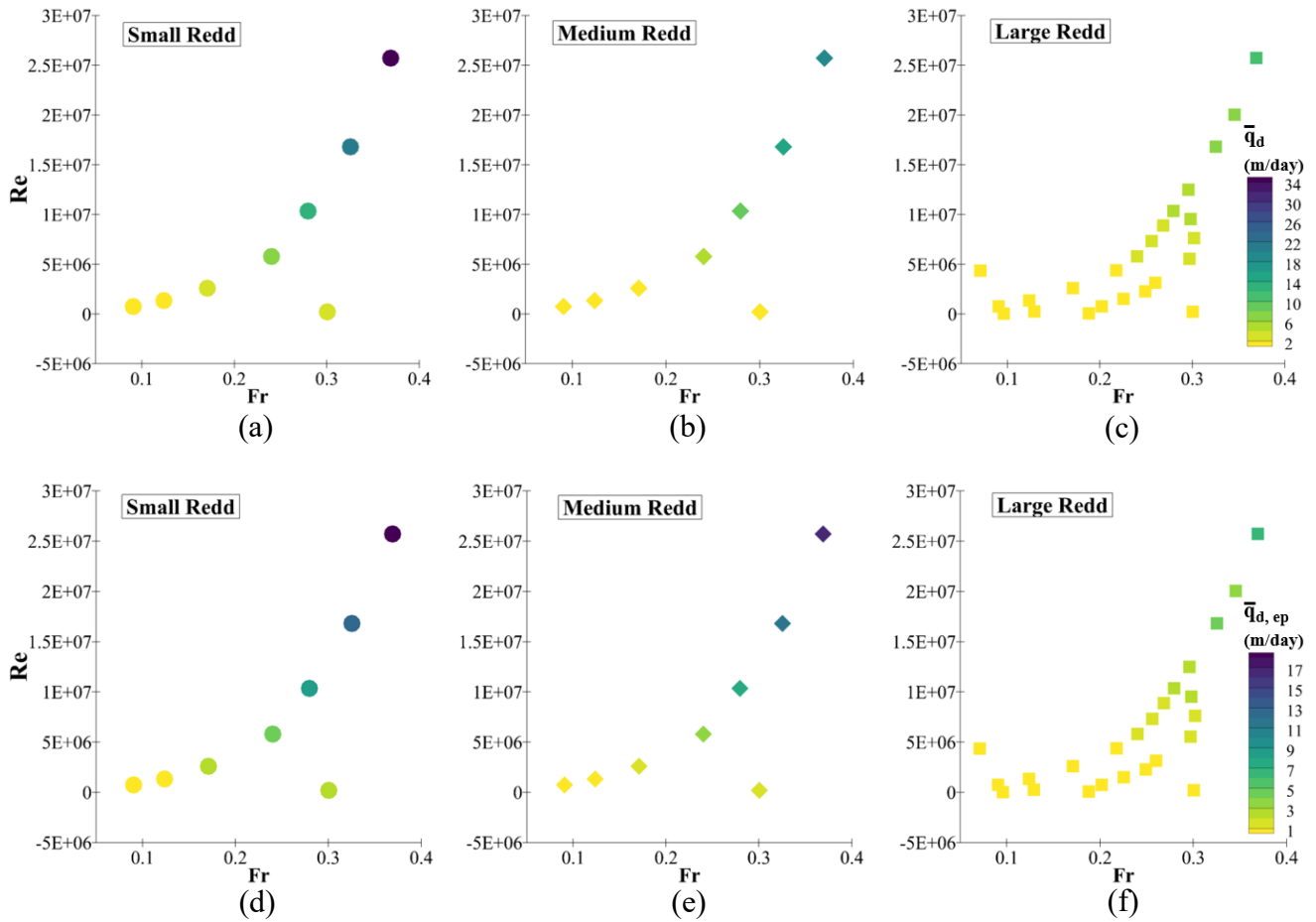
433 Figure 11: Normalized normal velocity distribution, $q^* = q/q_{max}$, (note y axes are not in the same
 434 scale to help visualize the lines), over a (a) small redd, (b) medium redd, and (c) large redd.

435



436
437
438
439

Figure 12: Subsurface flow characteristics for different surface hydrodynamics and three different redd sizes.



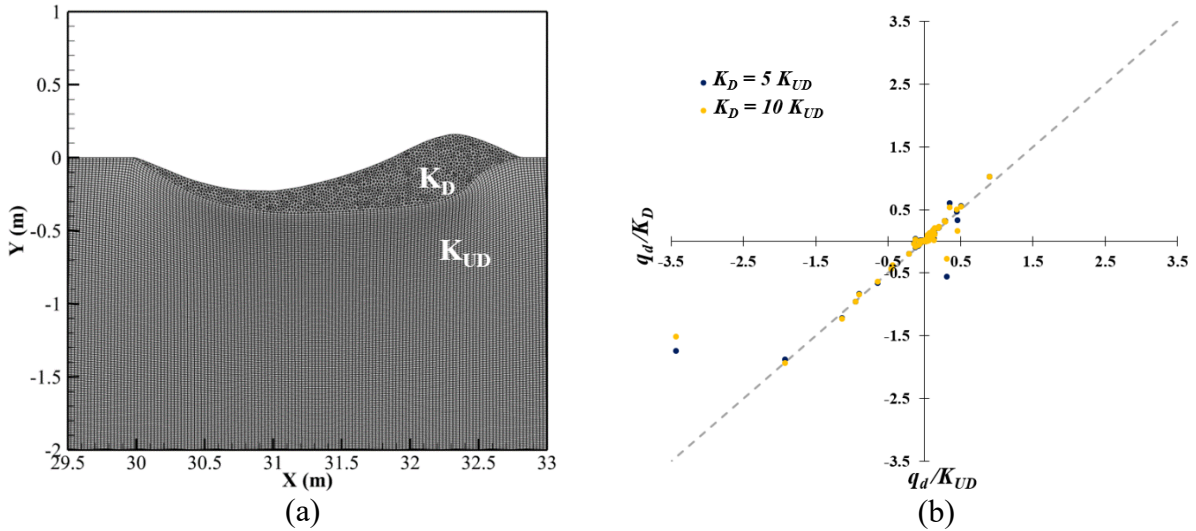
440
441

442
443

444 Figure 13: Averaged downwelling velocity over the redd (\bar{q}_d) (top panel) and between pit-tailspill
445 region affecting the egg pocket ($\bar{q}_{d,ep}$) (bottom panel) as a function of Reynolds Number (Re), Froude
446 Number (Fr), and Aspect Ratio (A_R).

447 7.3 Effect of categorical hydraulic conductivity

448 For Run 14 M (medium-sized redd), comparison of downwelling velocities between homogenous and
449 categorical heterogeneous hydraulic conductivities with 5 and 10 times larger hydraulic
450 conductivities in the redd than in the surrounding undisturbed sediment (Figure 14a) resulted in
451 similar dimensionless downwelling velocities (Figure 14b). This shows that the redd hydraulic
452 conductivity dominates the downwelling velocity and that the influence of heterogeneity between the
453 redd and surrounding sediment is negligible on the flow field within the redd. Spatially averaged
454 downwelling velocity over the redd and spatially averaged downwelling velocity going through the region
455 of the egg pocket chiefly scale linearly with the hydraulic conductivity.



456
457
458
459
460
461

Figure 14: (a) Redd disturbed and undisturbed sediment with their own hydraulic conductivities, K_D and K_{UD} , respectively. (b) Comparison between downwelling velocities normalized by the redd hydraulic conductivities for the homogeneous case (K_{UD}) and the heterogeneous ($K_D = 5 \cdot K_{UD}$ and $K_D = 10 \cdot K_{UD}$).

462 7.4 Regression predictive equations

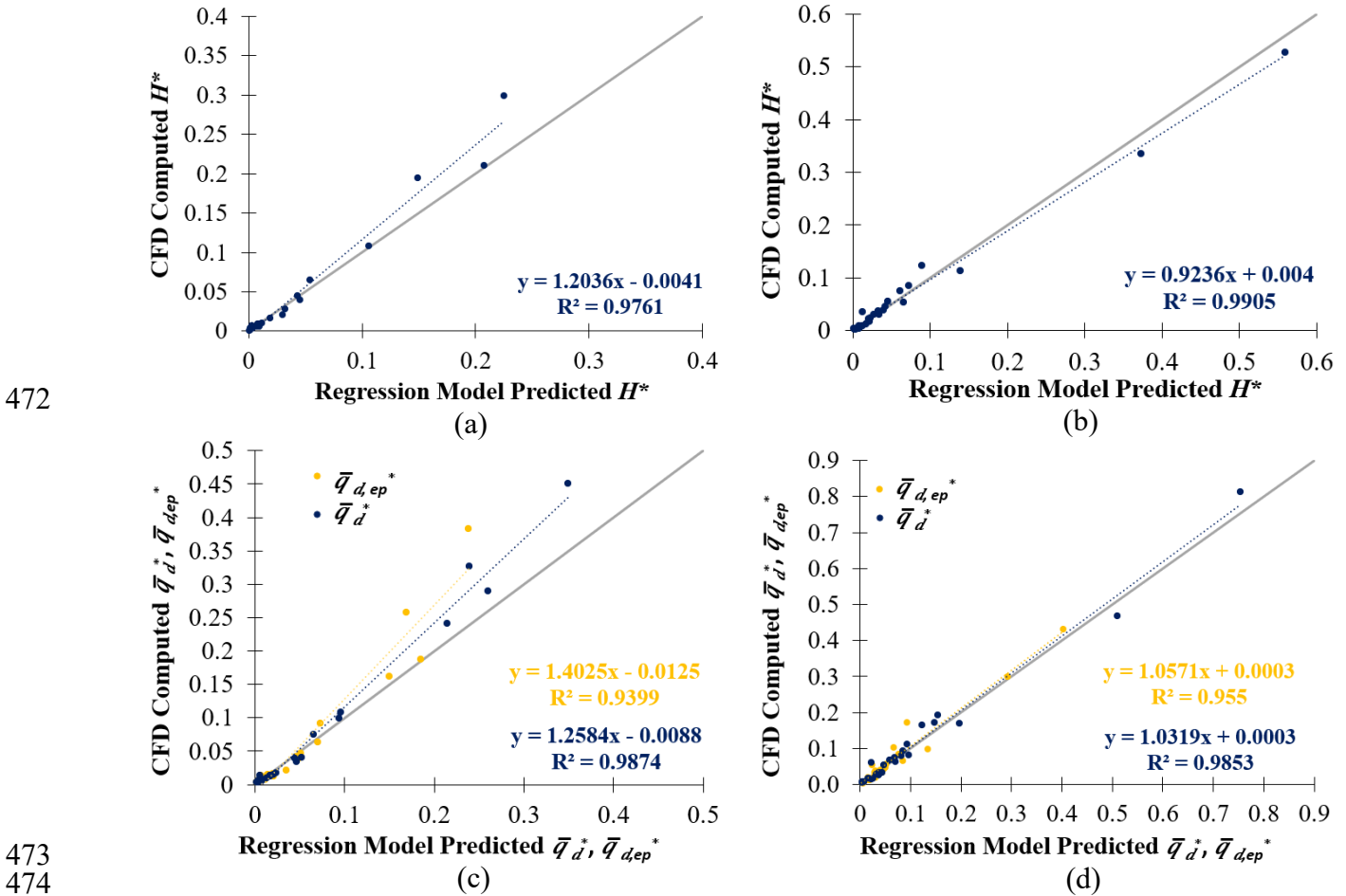
463 The dimensional analysis was applied to the 3 dependent variables: total head drop (ΔH_R),
464 downwelling velocity for the entire redd (\bar{q}_d), and downwelling velocity impacting only the egg
465 pocket ($\bar{q}_{d,ep}$). Linear regression analysis of the log-transformed dimensionless numbers showed that
466 Fr and Re , as well as A_R are statistically significant ($p < 0.01$), but the relative submergence was not
467 ($p \sim 0.8$), on both total head drop and downwelling flux. Thus, it was eliminated from the regression
468 analysis, resulting in three independent dimensionless quantities, Fr , Re , and A_R :

$$H^* = \frac{\Delta H_R}{L} = 0.122 \cdot (A_R)^{1.274} \cdot (Re)^{0.313} \cdot (Fr)^{2.219} \quad (4)$$

$$\bar{q}_d^* = \frac{\bar{q}_d}{K} = 0.052 \cdot (A_R)^{0.82} \cdot (Re)^{0.317} \cdot (Fr)^{1.91} \quad (5)$$

$$\bar{q}_{d,ep}^* = \frac{\bar{q}_{d,ep}}{K} = 0.112 \cdot (A_R)^{0.784} \cdot (Re)^{0.247} \cdot (Fr)^{1.91} \quad (6)$$

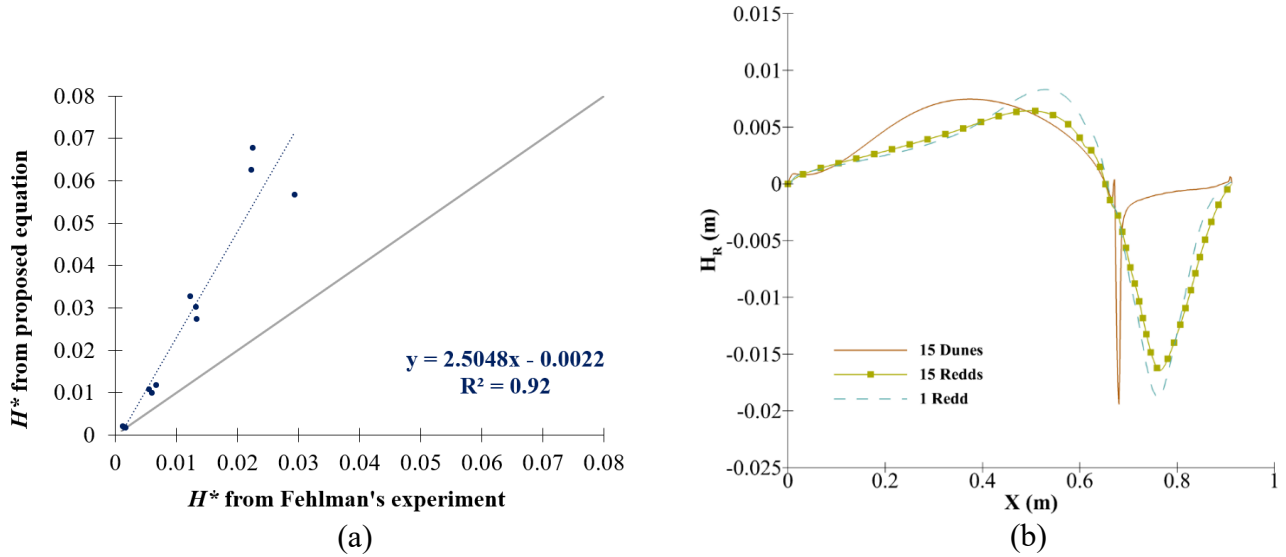
469 Comparisons of the model predictions against the independent data sets not used in the regression
 470 analysis showed very good performance with $R^2 > 0.9$ and strong correlations along the 1:1 line
 471 (Figure 15).



473
 474
 475 Figure 15: Linear regression plots for computed (y-axis) VS predicted (a) calibration and (b)
 476 validation of dimensionless total head drop across the redd. (c) Calibration and (d) validation of
 477 averaged downwelling velocities across the egg pocket (yellow) and entire redd (blue) for 48 runs (21
 478 calibration and 27 validation).

479 We also tested whether equation (4) can predict the total head drop over dunes, extending the work of
 480 Fehlman (1985) (Figure 16a). The comparison shows a good fit ($R^2 \sim 0.9$), but model predictions are
 481 2.5 times higher than those measured in Fehlman's experiments (Figure 16a). We ran a simulation
 482 with a sequence of redds and dunes for the flow conditions of Fehlman's (1985) run number 11 to test
 483 whether the presence of multiple redds would explain the difference. The three simulations (single

484 redd, a sequence of 15 redds, and a sequence of 15 dunes) generated similar pressure distributions
 485 with the single redd having a slightly higher drop (Figure 16b). These results show that the difference
 486 is due to the shape of the dune rather than the fact that redds are typically isolated features, and dunes
 487 are a succession of bedforms adjacent to one another (Figure 16b).



488
 489 Figure 16: (a) Total head drop normalized by the length of the dune ($\Delta H_R/L$) across the uniform
 490 bedform for the flow hydraulics used in Fehلمان's experiment for dunes using our proposed equation
 491 and (b) pressure distribution over a sequence of 15 dunes, a sequence of 15 redds, and one redd.

492 Note that the dramatic drop in relative head for the 15-dunes case, occurring around $x = 0.7$ m is due
 493 to the sharp edge at triangular dunes and a more appropriate minimum head value would be around -
 494 0.01 m rather than $-0.02 H_R$. This is a significant result because it implies that the proposed equation
 495 (4) can be extended to dunes by dividing H_R by a constant factor of 5 (2.5 times 2 where 2 accounts
 496 for semi-amplitude), resulting in semi-amplitude as given by equation (7) because Elliott and Brooks
 497 used semi-amplitude rather than amplitude:

$$498 \quad h_{dune} = \frac{0.122}{5} \cdot \left(\frac{A}{L}\right)^{1.274} \cdot (Re)^{0.313} \cdot (Fr)^{2.219} \quad (7)$$

499 where h_{dune} is the semi amplitude ($H^*/2$).

500 **8 DISCUSSION**

501 Our surface flow range is fairly extensive, encompassing spawning areas ranging from very shallow
502 to very deep flows, as well as slow and fast water. Because the depth and velocity quantities are not
503 independent as expressed through the resistance equation, e.g., Manning's equation, we did not keep
504 one constant and change the other arbitrarily; instead, we modified them both simultaneously because
505 an increase in discharge results in an increase in both velocity and depth. Our hydraulic scenarios also
506 aim to replicate what is observed in the field in locations near redds. River management teams
507 commonly use reach-averaged values, so the flow hydraulics used are reach-averaged values rather
508 than local flow velocities and depths over a specific redd.

509 We employed a VOF model that allows tracking of the free surface elevation, which helps to better
510 represent the pressure distribution at the water-sediment interface accurately. Most computational
511 fluid dynamics models have used a single-phase with a rigid-lid approximation. However, we used a
512 two-phase model (flow of the water column with air above it) because both hydrostatic and
513 nonhydrostatic-driven fluxes can significantly increase when compared to the rigid-lid approach
514 because we are analyzing surface flows within a wide range of Froude numbers (Lee et al., 2021), and
515 the deformation of the river's free surface may influence to redd-driven hyporheic exchange. The
516 fixed lid approach can be beneficial where no large changes in water surface elevations occur and
517 where the VOF method may be computationally expensive.

518 Our numerical modeling demonstrates the impact of salmon redd shape and size, as well as surface
519 discharge, on the hyporheic flow inside the redd, which directly influences the embryos. As seen in
520 earlier publications (Stonedahl et al., 2010; Wörman et al., 2007), multiscale hyporheic flows are
521 driven by the superposition of multiple scales of geomorphic features, and multi-cell hyporheic
522 exchange is formed when surface flows interact with a redd (Tonina & Buffington, 2009a). The near-
523 bed pressure distribution produces the largest flow circulation at the region between the redd pit

524 bottom and the crest, where eggs incubate. Other secondary hyporheic exchange cells whose
525 formation and relative size are dependent on flow hydraulics and redd aspect ratio, develop adjacent
526 to the large flow circulation. This large hyporheic exchange cell is always present and has a
527 downstream flow direction regardless of flow hydraulics or redd size, whereas the other smaller
528 hyporheic exchange cells develop and grow with higher discharges and larger A_R values and can
529 disappear with lower discharge and smaller A_R values. Another small cell is formed downstream of
530 the tailspill for the highest A_R , which develops in size as the discharge increases. The large, constant
531 cell, between the pit and the crest, is the most crucial for egg development as it supplies oxygen-rich
532 surface water to the egg pocket. The generated downwelling flux increases with discharge and aspect
533 ratio, suggesting that smaller redds with larger amplitudes may benefit from higher interstitial flows
534 more than large redds with smaller amplitudes.

535 For a given redd configuration, larger discharges with the same water temperature will supply more
536 oxygen-rich water to developing embryos as downwelling flux increases with discharge. This might
537 have an important implication in managing water resources from dam releases or water diversion
538 during the embryo's development. For oxygen delivery and consumption, however, both water
539 temperature and interstitial flow velocity are important during embryos' development stage (Martin et
540 al., 2020). In managed rivers such as the Sacramento River, high levels of water discharge can more
541 rapidly deplete cool water pools stored in dams and thus lead to elevated temperature exposure during
542 the embryonic period (Anderson et al., 2022). As a result, our findings should be interpreted in
543 combination with a biophysical model of oxygen supply and demand for developing embryos to fully
544 comprehend the significance of discharge for embryo survival (Martin et al., 2020).

545 When salmon spawn, they alter the morphology of the riverbed forming the typical dune-like redd
546 and increase the redd hydraulic conductivity compared to the surrounding undisturbed sediment and
547 thereby hyporheic exchange because spawning loosens the bed and washes particles from the gravels

548 (Chapman, 1988; Zimmermann & Lapointe, 2005a). This is beneficial to the embryos because this
549 increases the advection of dissolved oxygen and nutrients from the stream to the egg pocket.
550 Hydraulic conductivity in redds for chinook salmon was found to vary from $3 \cdot 10^{-2}$ m/s (Chapman et
551 al., 1986) to $1.5 \cdot 10^{-4}$ m/s (Geist, 2005; Malcolm et al., 2004) in unspawned beds. Here we show the
552 effect of categorical heterogeneity between a newly formed redd and undisturbed material that does
553 not focus downwelling flow. The hyporheic flows within the egg pocket are dominated by the redd
554 hydraulic conductivity regardless of the surrounding undisturbed condition. This result is supported
555 by earlier simulations of Tonina & Buffington (2009b), although they did not report this behavior.
556 This suggests that the reduction of the redd hydraulic properties over time from newly built redds
557 toward undisturbed material (Zimmermann & Lapointe, 2005a, 2005b) can be studied by reducing the
558 hydraulic conductivity of the homogeneous case. Thus, the advantage of the proposed normalization
559 of the downwelling fluxes by the redd hydraulic conductivity (equations 5, 6) is that it allows the
560 model to be applied to different permeabilities that may vary not only temporally but also among
561 redds.

562 The size and shape of salmon redd varies enormously both within and across species (Deverall et al.,
563 1993; Evenson, 2001; Tonina & Buffington, 2009a). However, the biological implications of this
564 phenotypic variability for oxygen supply to developing embryos has been unknown. Here, for the
565 first time, we quantified how redd size and shape influence interstitial flows within the redd. We
566 found that the effect of redd morphology and stream discharge on interstitial flow can be
567 characterized primarily by the aspect ratio of the redd, along with the Reynolds number and Froude
568 number. We found that the Reynolds number, Froude number and aspect ratio significantly affect
569 flow velocity within the redd using regression analysis, based on the subset of the 21 simulations that
570 encompass the varied sizes of redd and surface discharge. The size of the redd, the velocity of the
571 surface stream, and the depth of the flow are all represented by these variables. As Re increases, more

572 pressure builds up on the redd, which is then modulated by the Fr and A_R , causing hyporheic flow to
573 increase.

574 Flows across dunes, which have a similar form as redds, can be used to understand the influence of
575 the redd aspect ratio on hyporheic flows. Larger head gradients and faster pore water velocities are
576 produced by dunes with taller bedforms (Lee et al., 2020), just as they are found in our model for
577 redds with larger aspect ratios. The total head drop found in our model, which is about twice as large
578 as that reported in Fehلمان's (1985) experiment (Figure 16), might be attributed to the shape of the
579 redd with the pit and the hump (Figure 3 and Figure 7), while the impact of a single versus a sequence
580 of features has negligible effect. This allows us to propose a new equation for semi-amplitude head
581 drop around a dune bedform, which extends that of Elliott and Brooks (1997a) by accounting for the
582 dune aspect ratio and Reynolds number whose effects were not accounted for because of the narrow
583 range of hydraulic variability in Fehلمان's (1985) experiments.

584 One of the limitations of our study's separate domain analysis approach is that the pressure profile
585 obtained from the surface waterbed is used as the pressure inlet boundary condition for coupling the
586 surface and subsurface domains. (Broecker et al., 2019) found that not only does surface water
587 influence the subsurface, but the subsurface also influences the surface flow conditions. However, for
588 the range of hydraulic conductivity we used, the exchange in mass between surface and subsurface is
589 small and downwelling mass flux is less than 1% of the total mass transported by the surface flow.

590 **9 CONCLUSION**

591 Building on previous studies, we quantify the systematic change of hyporheic exchange induced by
592 the redd-stream flow interaction for a broad range of surface flow hydraulics and redd sizes. Our
593 simulations show that the total head gradient across the redd increases with the redd aspect ratio and
594 river discharge. Regardless of surface flow hydraulics, the shape of the total head distribution over

595 the redd stays typically similar, with the two lowest heads occurring at the beginning and crest of the
596 redd and a high head in between the pit and the tailspill. Simulations show another high total head
597 located on the streambed downstream of the redd, but its intensity decreases with redd aspect ratio
598 and disappears for the smallest aspect ratio (0.077) studied here.

599 The highest hyporheic fluxes occur in the redd near the egg pocket. This suggests that, by the way in
600 which they form their redds, salmonids actively enhance the environmental conditions of the egg
601 habitat. The spawning activities alter both streambed morphology and sediment permeability, which
602 after spawning activity, is higher in the redd than the surrounding sediment. The effect of altered
603 hydraulic conductivity can be chiefly captured using the homogenous hydraulic conductivity of the
604 disturbed sediment for the entire domain, e.g., redd and undisturbed material. This is because the
605 redd-induced pressure profile mainly keeps the flow lines within the shallow near-surface domain of
606 the disturbed sediment.

607 Based on dimensional analysis, our simulations allow identifying a set of regression equations, which
608 predict the total head drop and the mean downwelling hyporheic fluxes from three dimensionless
609 independent variables: the Reynolds number, the Froude number, and the redd aspect ratio. The
610 regression equation for the mean downwelling velocity in the egg pocket could be used to quantify
611 the hydraulic characteristics of the interstitial flows experienced by the egg and thus study an
612 embryo's habitat. The regression equation for the total head amplitude extends the range of
613 applicability of that proposed by Elliott and Brooks (1997b) based on Fehlman's (1985) dataset and
614 thus provides an important tool to study hyporheic processes induced by dune-like bedforms.

615 **Acknowledgement**

616 This research has been supported by the grant 19-028-300 California State Water Resources Control
617 Board. We would like to thank Andrew Pike who share the velocity-depth coupled at redd locations

618 along the Sacramento River quantified in the project Winter-run Chinook salmon Lifecycle model
619 project. All data have been reported in the hydroshare repository Bhattarai et al (2022),
620 <http://www.hydroshare.org/resource/6deaf594de954b95b81bd117bd919960>.

621 REFERENCES

- 622 Anderson, J. J., Beer, W. N., Israel, J. A., & Greene, S. (2022). Targeting river operations to the
623 critical thermal window of fish incubation: Model and case study on Sacramento River winter-
624 run Chinook salmon. *River Research and Applications*, 38(5), 895–905.
625 <https://doi.org/10.1002/rra.3965>
- 626 *ANSYS Fluent Theory Guide*. (2019). Retrieved from <http://www.ansys.com>
- 627 Bhattarai, B., D. Tonina, W. J. Reeder, R. Budwig, B. Hilliard, B. Martin, T. Xing (2022). Salmon
628 Redd induced Hyporheic Flow, HydroShare,
629 <http://www.hydroshare.org/resource/6deaf594de954b95b81bd117bd919960>
- 630 Bjornn, T. C., & Reiser, D. W. (1991). Habitat requirements of salmonids in streams. In W. R.
631 Meehan (Ed.), *Influence of forest and rangeland management on salmonid fishes and their*
632 *habitats* (pp. 83–138). Am. Fish. Soc. Spec. Publ. 19. Bethesda, Md.
- 633 Boano, F., Harvey, J. W., Marion, A., Packman, A. I., Revelli, R., Ridolfi, L., & Wörman, A. (2014).
634 Hyporheic flow and transport processes: Mechanisms, models, and biogeochemical implications.
635 *Reviews of Geophysics*, 52(4), 603–679. <https://doi.org/10.1002/2012RG000417>
- 636 Boyd, J. W., Oldenburg, E. W., & McMichael, G. A. (2010). Color photographic index of fall
637 chinook salmon embryonic development and accumulated thermal units. *PLoS ONE*, 5(7).
638 <https://doi.org/10.1371/journal.pone.0011877>
- 639 Broecker, T., Teuber, K., Gollo, V. S., Nützmänn, G., Lewandowski, J., & Hinkelmann, R. (2019).
640 Integral flow modelling approach for surface water-groundwater interactions along a rippled

641 streambed. *Water (Switzerland)*, 11(7). <https://doi.org/10.3390/w11071517>

642 Burner, C. J. (1951). Characteristics of spawning nests of Columbia River salmon. *Fishery Bulletin*,
643 52, 97–110.

644 Buxton, T. H., Buffington, J. M., Tonina, D., Fremier, A. K., & Yager, E. M. (2015). Modeling the
645 influence of salmon spawning on hyporheic exchange of marine-derived nutrients in gravel
646 stream beds. *Canadian Journal of Fisheries and Aquatic Sciences*, 72(8), 1146–1158.
647 <https://doi.org/10.1139/cjfas-2014-0413>

648 Buxton, T. H., Buffington, J. M., Yager, E. M., Hassan, M. A., & Fremier, A. K. (2015). The relative
649 stability of salmon redds and unspawned streambeds. *Water Resources Research*, 51(8), 6074–
650 6092. <https://doi.org/10.1002/2015WR016908>

651 Cardenas, Ford, A. E. A., Kaufman, M. H., Kessler, A. J., Cook, P. L. M., ... M. K.-J. of, & 2016, U.
652 (2016). Hyporheic flow and dissolved oxygen distribution in fish nests: The effects of open
653 channel velocity, permeability patterns, and groundwater upwelling. *Journal of Geophysical*
654 *Research: Biogeosciences*, 121(12), 3113–3130. <https://doi.org/10.1002/2016JG003381>

655 Cardenas, M. B., & Wilson, J. L. (2007a). Dunes, turbulent eddies, and interfacial exchange with
656 permeable sediments. *Water Resources Research*, 43(8), 1–16.
657 <https://doi.org/10.1029/2006WR005787>

658 Cardenas, M. B., & Wilson, J. L. (2007b). Exchange across a sediment–water interface with ambient
659 groundwater discharge. *Journal of Hydrology*, 346, 69–80.

660 Chapman, D. W. (1988). Critical review of variables used to define effects of fines in redds of large
661 salmonids. *Transactions of the American Fisheries Society*, 117(1), 1–21.

662 Chapman, D. W., Weitkamp, D. E., Welsh, T. L., Dell, M. B., & Schadt, T. H. (1986). Effects of
663 River Flow on the Distribution of Chinook Salmon Redds. *Transactions of the American*

664 *Fisheries Society*, 115(4), 537–547. <https://doi.org/10.1577/1548->
665 8659(1986)115<537:eorfot>2.0.co;2

666 Chen, X., Cardenas, M. B., & Chen, L. (2015). Three-dimensional versus two-dimensional bed form-
667 induced hyporheic exchange. *Water Resources Research*, 51, 2923–2936.
668 <https://doi.org/10.1002/2014WR016848>

669 Coble, D. W. (1961). Influence of water exchange and dissolved oxygen in redds on survival of
670 steelhead trout embryos. *Transactions of the American Fisheries Society*, 90, 469–474.

671 Cooper, A. C. (1965). The effect of transported stream sediments on the survival of sockeye and pink
672 salmon eggs and alevins. *Int. Pac. Salmon Fishery Commission Bulletin Bulletin*, (18), 18.

673 Crisp, D. T., & Carling, P. A. (1989). Observations on siting, dimensions, and structure of salmonid
674 redds. *Journal of Fish Biology*, 34, 119–134.

675 Deverall, K. R., Kelso, J. R. M., & James, G. D. (1993). Redd characteristics and implications for
676 survival of chinook salmon (*Oncorhynchus tshawytscha*) embryos in the Waitaki river, New
677 Zealand. *New Zealand Journal of Marine and Freshwater Research*, 27(4), 437–444.
678 <https://doi.org/10.1080/00288330.1993.9516585>

679 DeVries, P. (1997). Riverine salmonid egg burial depths: Review of published data and implications
680 for scour studies. *Canadian Journal of Fisheries and Aquatic Sciences*, 54(8), 1685–1698.
681 <https://doi.org/10.1139/f97-090>

682 DeVries, P. (2012). Salmonid influences on rivers: A geomorphic fish tail. *Geomorphology*, 157–158,
683 66–74. <https://doi.org/10.1016/j.geomorph.2011.04.040>

684 Elliott, A. H. (1990). *Transfer of solutes into and out of streambeds*. Pasadena, CA: WM Keck
685 Laboratory of Hydraulics and Water Resources, Calif. Inst. of Technol.

686 Elliott, A. H., & Brooks, N. H. (1997a). Transfer of nonsorbing solutes to a streambed with bed

687 forms: laboratory experiments. *Water Resources Research*, 33(1), 137–151.

688 Elliott, A. H., & Brooks, N. H. (1997b). Transfer of nonsorbing solutes to a streambed with bed
689 forms: Theory. *Water Resources Research*, 33(1), 123–136. <https://doi.org/10.1029/96WR02784>

690 Evenson, D. F. (2001). *Egg pocket depth and particle size composition within Chinook salmon redds*
691 *in the Trinity River, California*. Humboldt State University.

692 Fehلمان, H. M. (1985). Resistance Components and Velocity Distributions of Open Channel Flows
693 Over Bedforms.

694 Geist. (2005). A conceptual spawning habitat model to aid in ESA recovery plans for snake river fall
695 chinook salmon. *BPA Report DOE/BP, 00000652–2*(September), i–iii, 1–16.

696 Geist, & Dauble, D. D. (1998). Redd site selection and spawning habitat use by fall chinook salmon:
697 The importance of geomorphic features in large rivers. *Environmental Management*, 22(5), 655–
698 669. <https://doi.org/10.1007/s002679900137>

699 Groot, C., & Margolis, L. (1991). *Pacific salmon life histories*. Vancouver, Canada: Columbia Press.

700 Hassan, M. A., Tonina, D., & Buxton, T. H. (2015). Does small-bodied salmon spawning activity
701 enhance streambed mobility? *Water Resources Research*, 51(9), 7467–7484.
702 <https://doi.org/10.1002/2015WR017079>

703 Hendry, A. P., Morbey, Y. E., Berg, O. K., & Wenburg, J. K. (2004). Adaptive variation in
704 senescence: Reproductive lifespan in a wild salmon population. *Proceedings of the Royal*
705 *Society B: Biological Sciences*, 271(1536), 259–266. <https://doi.org/10.1098/rspb.2003.2600>

706 Hirt, C. W., & Nichols, B. D. (1981). Volume of fluid (VOF) method for the dynamics of free
707 boundaries. *Journal of Computational Physics*, 39, 201–225.

708 Janssen, F., Cardenas, M. B., Sawyer, A. H., Dammrich, T., Krietsch, J., & De Beer, D. (2012). A
709 comparative experimental and multiphysics computational fluid dynamics study of coupled

710 surface-subsurface flow in bed forms. *Water Resources Research*, 48(8), 1–16.
711 <https://doi.org/10.1029/2012WR011982>

712 Lee, A., Aubeneau, A. F., & Cardenas, M. B. (2020). The Sensitivity of Hyporheic Exchange to
713 Fractal Properties of Riverbeds. *Water Resources Research*, 56(5), 1–15.
714 <https://doi.org/10.1029/2019WR026560>

715 Lee, A., Aubeneau, A., Liu, X., & Cardenas, M. B. (2021). Hyporheic Exchange in Sand Dunes
716 Under a Freely Deforming River Water Surface. *Water Resources Research*, 57(3), 1–13.
717 <https://doi.org/10.1029/2020WR028817>

718 Malcolm, I. A., Soulsby, C., Youngson, A. F., Hannah, D. M., McLaren, I. S., & Thorne, A. (2004).
719 Hydrological influences on hyporheic water quality implications for salmon egg survival.
720 *Hydrological Processes*, 18(9), 1543–1560. <https://doi.org/10.1002/hyp.1405>

721 Martin, B. T., Pike, A., John, S. N., Hamda, N., Roberts, J., Lindley, S., & Danner, E. M. (2017).
722 Phenomenological vs. biophysical models of thermal stress in aquatic eggs. *Ecology Letters*,
723 20(1), 50–59.

724 Martin, B. T., Dudley, P. N., Kashef, N. S., Stafford, D. M., Reeder, W. J., Tonina, D., et al. (2020).
725 The biophysical basis of thermal tolerance in fish eggs: Thermal tolerance in fish eggs.
726 *Proceedings of the Royal Society B: Biological Sciences*, 287(1937).
727 <https://doi.org/10.1098/rspb.2020.1550>

728 Merz, J. E., Setka, J. D., Pasternack, G. B., & Wheaton, J. M. (2004). Predicting benefits of
729 spawning-habitat rehabilitation to salmonid (*Oncorhynchus* spp.) fry production in a regulated
730 California river. *Canadian Journal of Fisheries and Aquatic Sciences*, 61(8), 1433–1446.
731 <https://doi.org/10.1139/F04-077>

732 Meselhe, E. A., & Odgaard, A. J. (1998). 3D Numerical Flow Model for Fish Diversion Studies at
733 Wanapum Dam. *Journal of Hydraulic Engineering*, 124(12), 1203–1214.

734 [https://doi.org/10.1061/\(asce\)0733-9429\(1998\)124:12\(1203\)](https://doi.org/10.1061/(asce)0733-9429(1998)124:12(1203))

735 Monofy, A., & Boano, F. (2021). The Effect of Streamflow, Ambient Groundwater, and Sediment
736 Anisotropy on Hyporheic Zone Characteristics in Alternate Bars. *Water Resources Research*,
737 57(1), 1–22. <https://doi.org/10.1029/2019WR025069>

738 Monsalve, A., & Yager, E. M. (2017). Bed Surface Adjustments to Spatially Variable Flow in Low
739 Relative Submergence Regimes. *Water Resources Research*, 53(11), 9350–9367.
740 <https://doi.org/10.1002/2017WR020845>

741 Moreto, J. R., Reeder, W. J., Budwig, R., Tonina, D., & Liu, X. (2022). Experimentally Mapping
742 Water Surface Elevation, Velocity, and Pressure Fields of an Open Channel Flow Around a
743 Stalk. *Geophysical Research Letters*, 49(7), 1–10. <https://doi.org/10.1029/2021gl096835>

744 Moriasi, D. N., Arnold, J., Van Liew, M., Bingner, R., Harmel, D., & Veith, T. (2007). Model
745 evaluation guidelines for systematic quantification of accuracy in watershed simulations.
746 *Transactions of the American Society of Agricultural and Biological Engineers*, 50(3), 885–900.

747 Mueller, R. (2005). *Deepwater Spawning of Fall Chinook Salmon (Oncorhynchus tshawytscha) near*
748 *Ives and Pierce Island of the Columbia River, 2004-2005 Annual Report, Project No.*
749 *199900301*.

750 Reeder, W. J. J., Quick, A. M. A. M., Farrell, T. B. T. B., Benner, S. G. S. G., Feris, K. P. K. P., &
751 Tonina, D. (2018). Spatial and Temporal Dynamics of Dissolved Oxygen Concentrations and
752 Bioactivity in the Hyporheic Zone. *Water Resources Research*, 54(3), 2112–2128.
753 <https://doi.org/10.1002/2017WR021388>

754 Riebe, C. S., Sklar, L. S., Overstreet, B. T., & Wooster, J. K. (2014). Optimal reproduction in salmon
755 spawning substrates linked to grain size and fish length. *Water Resources Research*, 50(2), 898–
756 918. <https://doi.org/10.1002/2013WR014231>

- 757 Stonedahl, S. H., Harvey, J. W., Wörman, A., Salehin, M., & Packman, A. I. (2010). A multiscale
758 model for integrating hyporheic exchange from ripples to meanders. *Water Resources Research*,
759 46(12), 1–14. <https://doi.org/10.1029/2009WR008865>
- 760 Stuart, T. A. (1953a). *Spawning migration, reproduction and young stage of loch trout (Salmo trutta*
761 *L.). Freshwater and Salmon Fisheries Research*. Edinburgh, Scotland: Department of
762 Agriculture and Fisheries.
- 763 Stuart, T. A. (1953b). Water currents through permeable gravel and their significance to spawning
764 salmonids, etc. *Nature*, 172, 407–408.
- 765 Tappel, P. D., & Bjornn, T. C. (1983). A New Method of Relating Size of Spawning Gravel to
766 Salmonid Embryo Survival. *North American Journal of Fisheries Management*, 3(2), 123–135.
767 [https://doi.org/10.1577/1548-8659\(1983\)3<123:anmors>2.0.co;2](https://doi.org/10.1577/1548-8659(1983)3<123:anmors>2.0.co;2)
- 768 Tonina, D., & Buffington, J. M. (2009a). A three-dimensional model for analyzing the effects of
769 salmon redds on hyporheic exchange and egg pocket habitat. *Canadian Journal of Fisheries and*
770 *Aquatic Sciences*, 66(12), 2157–2173. <https://doi.org/10.1139/F09-146>
- 771 Tonina, D., & Buffington, J. M. (2009b). Hyporheic exchange in mountain rivers I: Mechanics and
772 environmental effects. *Geography Compass*, 3(3), 1063–1086. [https://doi.org/10.1111/j.1749-](https://doi.org/10.1111/j.1749-8198.2009.00226.x)
773 [8198.2009.00226.x](https://doi.org/10.1111/j.1749-8198.2009.00226.x)
- 774 Trauth, N., Schmidt, C., Maier, U., Vieweg, M., & Fleckenstein, J. H. (2013). Coupled 3-D stream
775 flow and hyporheic flow model under varying stream and ambient groundwater flow conditions
776 in a pool-riffle system. *Water Resources Research*, 49(9), 5834–5850.
777 <https://doi.org/10.1002/wrcr.20442>
- 778 Wilson, R. V., Stern, F., Coleman, H. W., & Paterson, E. G. (2001). Comprehensive approach to
779 verification and validation of CFD simulations—Part 2: Application for rans simulation of a
780 cargo/container ship. *Journal of Fluids Engineering, Transactions of the ASME*, 123(4), 803–

781 810. <https://doi.org/10.1115/1.1412236>

782 Wörman, A., Packman, A. I., Marklund, L., Harvey, J. W., & Stone, S. H. (2007). Fractal topography
783 and subsurface water flows from fluvial bedforms to the continental shield. *Geophysical*
784 *Research Letters*, 34(7), 1–5. <https://doi.org/10.1029/2007GL029426>

785 Xing, T., & Stern, F. (2010). Factors of safety for Richardson extrapolation. *Journal of Fluids*
786 *Engineering, Transactions of the ASME*, 132(6), 0614031–0640313.
787 <https://doi.org/10.1115/1.4001771>

788 Xing, T., & Stern, F. (2011). Closure to “discussion of ‘factors of safety for Richardson
789 Extrapolation’” (2011, ASME J. Fluids Eng., 133, p. 115501). *Journal of Fluids Engineering,*
790 *Transactions of the ASME*, 133(11), 2–7. <https://doi.org/10.1115/1.4005030>

791 Xing, T., Carrica, P., & Stern, F. (2008). Computational towing tank procedures for single run curves
792 of resistance and propulsion. *Journal of Fluids Engineering, Transactions of the ASME*, 130(10),
793 1011021–10110214. <https://doi.org/10.1115/1.2969649>

794 Yates, D., Galbraith, H., Purkey, D., Huber-Lee, A., Sieber, J., West, J., et al. (2008). Climate
795 warming, water storage, and Chinook salmon in California’s Sacramento Valley. *Climatic*
796 *Change*, 91(3–4), 335–350. <https://doi.org/10.1007/s10584-008-9427-8>

797 Zimmermann, A. E., & Lapointe, M. (2005a). Intergranular flow velocity through salmonid redds:
798 Sensitivity to fines infiltration from low intensity sediment transport events. *River Research and*
799 *Applications*, 21(8), 865–881. <https://doi.org/10.1002/rra.856>

800 Zimmermann, A. E., & Lapointe, M. F. (2005b). Sediment infiltration traps: Their use to monitor
801 salmonid spawning habitat in headwater tributaries of the Cascapédia River, Québec.
802 *Hydrological Processes*, 19(20), 4161–4177. <https://doi.org/10.1002/hyp.5879>